



Consistency of the Infrared Variability of Sgr A* over 22 yr

Zhuo Chen^{1,11} , E. Gallego-Cano^{2,3,11} , T. Do^{1,11} , G. Witzel^{1,4,11} , A. M. Ghez^{1,11} , R. Schödel^{2,11}, B. N. Sitarski^{1,5,11},
E. E. Becklin^{1,11}, J. Lu^{6,11} , M. R. Morris^{1,11} , A. Dehghanfar^{1,7,11} , A. K. Gautam^{1,11} , A. Hees^{1,8,11} ,
M. W. Hosek, Jr.^{1,11} , S. Jia^{6,11} , A. C. Mangian^{9,11} , and K. Matthews^{10,11}

¹ Department of Physics and Astronomy, UCLA, USA

² Instituto de Astrofísica de Andalucía (CSIC), Glorieta de la Astronomía s/n, E-18008 Granada, Spain

³ Centro Astronómico Hispano-Alemán (CSIC-MPG), Observatorio Astronómico de Calar Alto, Sierra de los Filabres, 04550, Gérgal, Almería, Spain

⁴ Max Planck Institute for Radio Astronomy, Auf dem Hügel 69, D-53121 Bonn (Endenich), Germany

⁵ Giant Magellan Telescope Corporation, Pasadena, CA, USA

⁶ Department of Astronomy, UC Berkeley, USA

⁷ Institut de Planetologie et d'Astrophysique de Grenoble, 414 Rue de la Piscine, F-38400 Saint-Martin-d'Heres, France

⁸ SYRTE, Observatoire de Paris, Université PSL, CNRS, Sorbonne Université, LNE, 61 avenue de l'Observatoire F-75014 Paris, France

⁹ Department of Astronomy, University of Illinois, Urbana-Champaign, USA

¹⁰ Division of Physics, Mathematics, and Astronomy, California Institute of Technology, USA

Received 2019 June 22; revised 2019 July 30; accepted 2019 August 17; published 2019 September 11

Abstract

We report new infrared (IR) measurements of the supermassive black hole at the Galactic Center, Sgr A*, over a decade that was previously inaccessible at these wavelengths. This enables a variability study that addresses variability timescales that are 10 times longer than earlier published studies. Sgr A* was initially detected in the near-infrared (NIR) with adaptive optics observations in 2002. While earlier data exists in form of speckle imaging (1995–2005), Sgr A* was not detected in the initial analysis. Here, we improved our speckle holography analysis techniques. This has improved the sensitivity of the resulting speckle images by up to a factor of three. Sgr A* is now detectable in the majority of epochs covering 7 yr. The brightness of Sgr A* in the speckle data has an average observed K magnitude of 16.0, which corresponds to a dereddened flux density of 3.4 mJy. Furthermore, the flat power spectral density of Sgr A* between ~ 80 days and 7 yr shows its uncorrelation in time beyond the proposed single power-law break of ~ 245 minutes. We report that the brightness and its variability is consistent over 22 yr. This analysis is based on simulations using the Witzel et al. model to characterize IR variability from 2006 to 2016. Finally, we note that the 2001 periape of the extended, dusty object G1 had no apparent effect on the NIR emission from accretion flow onto Sgr A*. The result is consistent with G1 being a self-gravitating object rather than a disrupting gas cloud.

Key words: accretion, accretion disks – black hole physics – Galaxy: center – techniques: high angular resolution

1. Introduction

The Galactic Center (GC), approximately 8 kpc (Reid 1993) from Earth, is host to the closest known supermassive black hole (SMBH; Ghez et al. 1998, 2000, 2005b, 2008; Schödel et al. 2002; Gillessen et al. 2009, 2017; Boehle et al. 2016). This makes it an excellent laboratory for studying the accretion properties of SMBHs. The accretion flow onto the SMBH at the GC gives rise to its radiative counterpart, Sgr A*, which appears to be very under-luminous compared to active galactic nuclei (AGNs) with comparable masses (Melia & Falcke 2001). Several different theoretical models have been developed to describe Sgr A*'s accretion flow, including the well-known advection-dominated accretion flow model (Ichimaru 1977; Narayan & Yi 1994; Abramowicz et al. 1995; Narayan et al. 1995) and the radiatively inefficient accretion flow model (RIAF; Yuan et al. 2003), both of which account for the low efficiency of the radiation loss of accreting gas and imply a hot and geometrically thick accretion structure.

An additional complexity and opportunity for modeling Sgr A* emission is that it is a variable source. Thus far the near-infrared (NIR) has proven to be a powerful window for characterizing Sgr A*'s variability (Witzel et al. 2018). Sgr A* was first detected in the NIR in 2002 with the first adaptive optics (AO) measurements of the GC (Genzel et al. 2003; Ghez et al. 2004). The NIR

short-term variability of Sgr A* is well characterized as a red-noise process (Press 1978). A power-law power spectral density (PSD) with a slope $\gamma_1 \approx 2$ can describe the variability on short timescales of minutes to hours (Do et al. 2009; Dodds-Eden et al. 2011; Witzel et al. 2012; Hora et al. 2014; Meyer et al. 2014). Witzel et al. (2018) reported a break in the PSD at a timescale of $\tau_b = 245_{-61}^{+88}$ minutes, which constitutes the characteristic timescale of the variability process. The power law and break timescales have been a powerful way to study black hole accretion physics over a large range of luminosity and mass scales (e.g., Eckart et al. 2006; Meyer et al. 2008, 2009; Do et al. 2009). Thus far, the longest NIR timescale of Sgr A* that has been measured is 1.9 yr (Meyer et al. 2009).

Prior to and during the epoch when AO systems were coming online (2002–2005, the Very Large Telescope), the GC was studied at high angular resolution comparable to that achieved with AO at NIR wavelengths with speckle data from 1995 to 2005 at Keck. The initial analysis used the shift-and-add technique (SAA; Eckart et al. 1995; Eckart & Genzel 1996; Ghez et al. 1998, 2000, 2005a; Hornstein et al. 2002; Lu et al. 2005; Rafelski et al. 2007). Sgr A* was not detected at this time owing to both the poorer sensitivity of these maps, which typically had detection limits ($\langle K_{\text{lim}} \rangle = 15.7$ mag; Boehle et al. 2016) comparable to or fainter than the average Sgr A* brightness ($\langle K_{\text{SgrA*}, \text{AO}} \rangle = 16.1$ mag; see Section 4.2), and the short time baseline of observations, which allowed only limited knowledge of the orbits

¹¹ Galactic Center Collaboration (GCC).

of nearby stars and the position of Sgr A* (Hornstein et al. 2002). Recently, the analysis of the speckle data has been improved with the speckle holography technique (Primot et al. 1990; Schödel et al. 2013; Boehle et al. 2016) to study two short-period stars, S0-38 and S0-2. This technique deepens the detection magnitude to $K < 17$ and opens up the possibility of detecting Sgr A* over a much longer time baseline.

Detecting Sgr A* during the speckle era (1995–2005) also extends the time baseline for discrete accretion events searches. Of particular interest is the spatially resolved dusty source G1, which underwent a tidal interaction with the central black hole as it went through periaipse in 2001 (Sitariski et al. 2014; Pfuhl et al. 2015; Witzel et al. 2017). This event may have increased the gas accretion onto Sgr A*. This object is similar observationally to G2, a cold, gaseous, highly eccentric object orbiting Sgr A* that reached closest approach in early 2014 (Gillessen et al. 2012). G2 was originally posited to be a 3 Earth-mass pure gas cloud that would measurably impact the accretion flow and variability process as it was tidally sheared from the moment of periaipse to ~ 7 yr after periaipse. However, no indication of this impact has so far been observed (e.g., Hora et al. 2014; Witzel et al. 2014, 2017, 2018; Pfuhl et al. 2015; Valencia-S et al. 2015), but the interaction phase may extend a few years (~ 7 yr or more) beyond periaipse passage (e.g., Pfuhl et al. 2015). One hypothesis is that G1 and G2 are part of the same gas streamer (Pfuhl et al. 2015). If this is the case, then G1 may have also impacted the accretion flow and thereby caused an enhancement of accretion luminosity as it went through closest approach to Sgr A*, and perhaps a few years after. While the AO measurements only started in 2002 and did not cover the time baseline of G1’s periaipse, the speckle data sets allow us to study whether G1 had any impact on the accretion flow related to its periaipse passage. Moreover, two short-period stars, S0-2 and S0-16, went through the periaipse (S0-16, 2000; S0-2, 2002) during the speckle era explored in this work, allowing us to test whether they had any kind of impact on the variability of Sgr A*.

In this work, we further develop the speckle holography technique to analyze our speckle data sets (1995–2005). We make the first report of NIR detection of Sgr A* prior to 2002. The details of the 10 years of data used in this work are described in Section 2. Section 3 presents the data analysis and methods, including the speckle holography image reconstruction and improvements, point sources extraction, photometric calibration, and Sgr A* identification from speckle holography images. Section 4 presents the results of Sgr A* detections, observed brightness, and its variability. Section 5 discusses the impact of G1’s periaipse, and also simulations to explore how the variability of Sgr A* in the speckle data is compared to that at later times. We conclude with a summary in Section 6 of the long-term activity of Sgr A* on timescales that are significantly longer than previous studies. Appendices A and B present details of photometry and source analyses used in this work for speckle holography images.

2. Data Sets

This Letter is based on speckle imaging that was taken as part of the Galactic Center Orbit Initiative (GCOI) and that was originally presented in Ghez et al. (1998, 2000, 2005a, 2008), Lu et al. (2005), Rafelski et al. (2007), and Boehle et al. (2016). From 1995 to 2005, the $K[2.2 \mu\text{m}]$ -band speckle data sets of the Galaxy’s central $\sim 5'' \times 5''$ region were obtained with the

W. M. Keck I 10 m telescope and its NIR camera (NIRC; Matthews & Soifer 1994; Matthews et al. 1996). During each epoch, which combine observations ranging from 1 to 4 nights, roughly 10,000 short-exposure frames ($t_{\text{exp}} = 0.1$ s) were obtained in datacubes consisting of 128 frames, which was the maximum number of frames that could be obtained in a single NIRC FITS file. Within each datacube, the time delay between the start time of each frame was 1.5 s in 1995 and 0.61 s thereafter. These series of short exposures were obtained with NIRC in its fine plate scale mode, with a scale of 20.396 ± 0.042 mas pixel $^{-1}$ and a corresponding field of view of $5''.22 \times 5''.22$. The data were obtained with the telescope in stationary mode, which keeps the pupil fixed with respect to the detector and causes the sky to rotate over a datacube. Our starting point for this Letter’s analysis is the individual frames that have had the instrumental effects removed (i.e., sky-subtracted, flat-fielded, bad-pixel-corrected, distortion-corrected) and that have been rotated to have a position angle of 0° on the plane of the sky (see details in Ghez et al. 1998, 2000). Table 1 summarizes the 27 speckle observation epochs.

3. Data Analysis and Methods

3.1. Image Reconstruction—A New Implementation of Speckle Holography

For this project, we have developed a new implementation of speckle holography. This builds on the work of Schödel et al. (2013), which has been applied to the GCOI data sets presented in Meyer et al. (2012; version 2_0) and Boehle et al. (2016; version 2_1) to study the short-period stars. In theory, the speckle holography technique uses the instantaneous PSF, which is measured from a set of reference sources, to deconvolve, in Fourier space, the distorted images and realize the contribution of all speckle information to the final diffraction-limited core, as follows:

$$O = \frac{\langle I_m P_m^* \rangle}{\langle |P_m|^2 \rangle} \quad (1)$$

where O is the Fourier transform of the object, I_m and P_m are the Fourier transforms of the m th short-exposure image and of its instantaneous PSF, respectively, and the brackets denote the mean over N frames. P_m^* is the conjugate complex of P_m (Primot et al. 1990).

In practice, speckle holography images are constructed through an iterative process. A key component of this analysis uses the PSF fitting program StarFinder (Diolaiti et al. 2000; also see Section 3.2). Below we detail the steps to construct the speckle holography images (version 2_2), and show how they differ from the implementation used in Boehle et al. (2016; version 2_1).

1. Shift all short-exposure frames to align the brightest speckle of IRS 16C. Subtract a constant background, which is estimated for each individual frame, from each short-exposure frame for version 2_2.
2. Rebin the speckle frames from original 20 mas pixel $^{-1}$ scale down to 10 mas pixel $^{-1}$ scale. Bilinear and cubic interpolation are used in version 2_1 and version 2_2, respectively.
3. Combine and construct an SAA image from all datacubes per observing epoch.

Table 1
Summary of Speckle Holography Observations^a

Date		Frames Used	K_{lim}^b (mag)	N_{Real}	N_{pix}^c	Sgr A* Pos. with Respect to Field of View (FoV) ^e		Original Refs. ^f	K Systematic Phot. Zero-point Error ^g (mag)	K Relative Phot. Error ^h (mag)
(U.T.)	(Decimal)					$\Delta\text{R.A.}$ (arcsec)	$\Delta\text{Decl.}$ (arcsec)			
1995 Jun 9–12	1995.439	5265	17.0	41	108042	−0.52	0.01	1	0.24	0.04
1996 Jun 26–27	1996.485	2283	15.8	49	82505	−1.22	−0.29	1	0.14	0.09
1997 May 14	1997.367	3426	16.8	51	92467	−0.90	−0.15	1	0.09	0.03
1998 Apr 2–3	1998.251	1718	15.8	39	95816	−0.57	−0.15	2	0.07	0.06
1998 May 14–15	1998.366	7675	16.8	45	102328	−0.45	−0.10	2	0.17	0.04
1998 Jul 3–5	1998.505	2040	16.4	43	116557	0.04	0.00	2	0.18	0.05
1998 Aug 4–6	1998.590	11032	17.1	47	109269	−0.41	0.04	2	0.18	0.04
1998 Oct 9, 11	1998.771	2000	16.6	45	97215	0.80	0.05	2	0.12	0.03
1999 May 2–4	1999.333	9423	17.2	52	107882	−0.45	−0.21	2	0.12	0.06
1999 Jul 24–25	1999.559	5690	17.4	54	100567	−0.46	−0.09	2	0.11	0.04
2000 Apr 21	2000.305	651	15.7	56	96248	0.84	0.11	3	0.09	0.04
2000 May 19–20	2000.381	15581	17.5	55	96853	−0.74	−0.24	3	0.08	0.03
2000 Jul 19–20	2000.584	10668	17.0	63	86452	−0.93	−0.12	3	0.15	0.04
2000 Oct 18	2000.797	2215	16.2	52	82315	−0.80	−0.42	3	0.09	0.05
2001 May 7–9	2001.351	6662	17.2	64	85028	−0.46	−0.20	3	0.17	0.02
2001 Jul 28–29	2001.572	6634	17.4	74	96872	−0.15	−0.22	3	0.15	0.02
2002 Apr 23–24	2002.309	13440	17.5	74	96953	−0.59	−0.17	3	0.12	0.05
2002 May 23–24	2002.391	11834	17.6	72	98552	−0.85	−0.08	3	0.14	0.05
2002 Jul 19–20	2002.547	4139	16.8	69	99994	−0.63	−0.39	3	0.17	0.05
2003 Apr 21–22	2003.303	3644	16.4	58	90963	−0.32	−0.40	3	0.18	0.06
2003 Jul 22–23	2003.554	2894	16.8	65	87265	−0.54	−0.24	3	0.08	0.01
2003 Sep 7–8	2003.682	6296	17.1	74	95367	−0.53	−0.44	3	0.14	0.03
2004 Apr 29–30	2004.327	6169	16.8	58	125423	−0.71	−0.21	4	0.17	0.04
2004 Jul 25–26	2004.564	13071	17.4	80	99819	−0.61	−0.41	4	0.15	0.04
2004 Aug 29	2004.660	2284	16.8	63	96172	−0.09	0.66	4	0.14	0.02
2005 Apr 24–25	2005.312	9553	17.1	70	105715	−0.36	−0.16	5	0.14	0.05
2005 Jul 26–27	2005.566	5606	16.8	84	108360	−0.26	−0.41	5	0.12	0.04

Notes.

^a All numbers given in the table are based on speckle holography version 2_2 (see Section 3).

^b K_{lim} is the magnitude that corresponds to the 95th percentile of all K magnitudes in the sample of real stars in the central $2'' \times 2''$ region (see Appendix B.1).

^c N_{pix} refers to the number of pixels in a given image that meet a 0.8 of maximum frames used criteria.

^d N_{ref} refers to the number of reference stars used to align the epoch of data.

^e The center of the FoV is the weighted average of the detector pixels, with the weight being the number of frames used squared at each pixel in the final image. The offsets reported above are $(x_{\text{SgrA*}} - x_{\text{centerFoV}})$.

^f 1: Ghez et al. (1998); 2: Ghez et al. (2000); 3: Ghez et al. (2005a); 4: Lu et al. (2005); 5: Rafelski et al. (2007).

^g Systematic photometric zero-point errors were calculated after performing initial photometric system calibration described in Appendix A.1. The average zero-point uncertainty $\bar{\sigma}_{\text{zp}}$ is 0.14 mag in NIRC K bandpass.

^h Relative photometric zero-point errors were determined by the relative photometry calibration using the stable calibrators (see Appendix A.2). The average zero-point uncertainty $\bar{\sigma}_{\text{zp}}$ for the relative photometry is 0.04 mag in NIRC K bandpass.

4. Extract astrometry and photometry of stars in the SAA images with StarFinder to identify potential PSF reference stars for the speckle holography analysis.
5. Select the brightest isolated sources as PSF reference stars for speckle holography. Each datacube typically has two to five reference sources (IRS 16NE, IRS 16C, IRS 16NW, IRS 16SW, IRS 33N), depending on the centering and image quality of the datacube.
6. Estimate the instantaneous PSF for each speckle frame from the median of the aligned and flux-normalized images of the reference stars. For each PSF, we subtract a constant value

- of $b_g + n \times \sigma$ ($n = 3$ for speckle images), where b_g is the background and σ is the noise. All resulting negative values in the PSF are set to 0. As a final step, a circular mask is applied to the PSF and the PSF is normalized to a total flux of 1. In version 2_2, we fixed a bug in StarFinder in which secondary stars that are not PSF reference stars were not being subtracted from the primary reference stars.
7. Improve the PSF estimate by subtracting all known secondary contaminating sources near the reference stars in each frame, using the preliminary PSFs from step (6) and information from step (4).

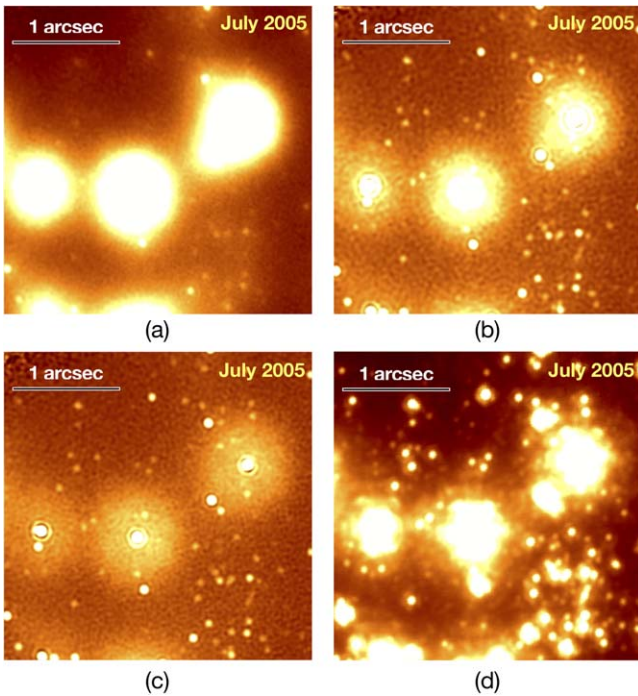


Figure 1. Comparison of the different high angular resolution techniques used to image the GC. The early data has been analyzed with (a) SAA, (b) the original implementation of speckle holography (version 2_1), and (c) the new implementation presented in this work (version 2_2). AO data taken at a similar time is shown in (d). The new speckle holography improves the sensitivity of the final images by up to a factor of three compared to the initial speckle holography.

8. Estimate the object Fourier transform O by applying Equation (1).
9. Apodize O with a model for the optical transfer function (OTF) of the telescope. Here we use a Gaussian function for 10 m aperture.
10. Reconstruct the image with inverse Fourier transform.
11. Repeat of the process from step (4) with the holographically reconstructed image, which has significantly higher quality than the initial SAA image.
12. Create multiple images for error estimation. In version 2_1, the data set for each epoch is divided into three equal-quality subsets to produce three speckle holography maps. In version 2_2, we use a bootstrapping method to produce 100 bootstrap data sets using sampling with replacement resulting in 100 speckle holography images produced from the same number of frames as the original data set.

The most important improvements of version 2_2 compared to version 2_1 are listed here.

1. Subtracting a constant sky background from each frame results in less background variation in the combined images, and in significantly suppressed edge effects near the edge of the FoV (Step 1).
2. Version 2_1 only used IRS 16C as PSF reference source. Version 2_2 uses up to five stars as PSF reference sources, depending on the instantaneous FoV (Step 5).
3. The bootstrapping method results in a more robust estimate of the astrometric and photometric uncertainties (Step 12).

Figure 1 shows the central region of the final reconstructed image from 2005 July. Compared to the earlier implementation

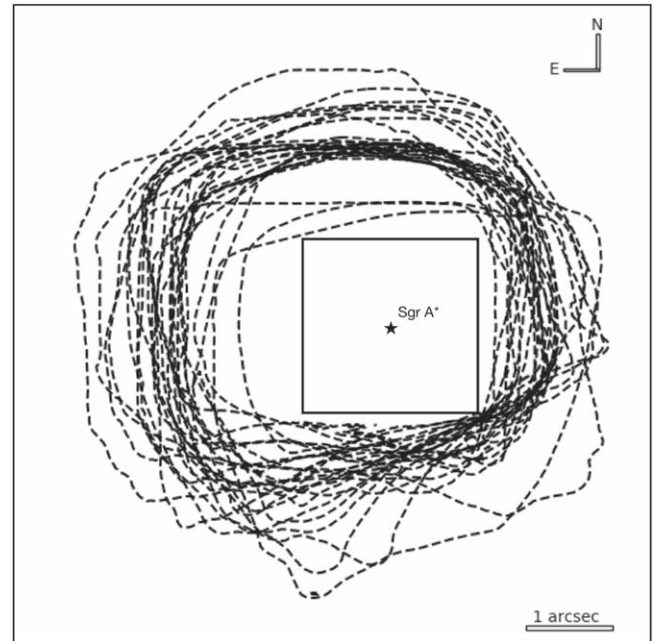


Figure 2. Comparison of the FoV for all the final speckle holography images. The dashed contours display the covered region for each epoch with contribution of over 80% of the individual frames. In order to minimize the edge effects, this study considers only the central $2'' \times 2''$ region center around Sgr A* outlined with the solid line.

of speckle holography and SAA analysis, the new analysis (version 2_2) has both improved the image quality and reduced the edge-effect artifacts.

3.2. Point Sources Extraction from Speckle Holography Images

Point sources are extracted from each epoch's final reconstructed image using StarFinder. Here, like in Section 3.1, we use the version of StarFinder utilized in Boehle et al. (2016) setting the cross-correlation threshold to 0.8, and a slightly lower minimum signal-to-noise ratio cut (3σ , versus 5σ). In order to estimate the astrometric and photometric uncertainties for the sources extracted, we perform StarFinder on 100 bootstrap images for each epoch and then calculate the standard deviation.

In order to minimize the impact of edge effects of speckle holography images, we restricted our analysis in the central $2'' \times 2''$ region center around Sgr A* for all epochs in the rest of this work. Owing to the observing strategy, in which stationary mode was used (see Section 2), the final image has significant variations in the number of individual frames that contributes to the each pixel toward the outer edge of the image. See contours in Figure 2.

Because speckle holography is a Fourier deconvolution technique, point-like artifacts can be produced in the middle of the FoV from edge effects, background, and PSF extraction. We therefore require sources to be detected above a minimum threshold number of bootstrap images to be considered real. This threshold is set by demanding that the probability of fake detections be less than 1% (see Appendix B.1). The bootstrap threshold for each epoch is reported in Table 2 and with an average of $10\% \pm 7\%$.¹²

¹² We note that this threshold is lower than in other GCOI studies because we have strong prior knowledge of the source (Sgr A*) location.

Table 2
Summary of Sgr A* Measurements

Date(UT)	Date (Epoch)	Bootstrap Fraction Cut ^a	Source Detection Limit ^b (mag)	Source Confusion with Sgr A*	<i>K</i> (mag)	<i>K</i> Error (mag)	Dereddened Flux (mJy)	Dereddened Flux Error (mJy)	Fraction of Bootstraps Detected	ΔT^c (minutes)
1995 Jun 9–12	1995.439	0.26	17.0	S0-19
1996 Jun 26–27	1996.485	0.24	16.0
1997 May 14	1997.367	0.22	16.9
1998 Apr 2–3	1998.251	0.14	15.8	...	15.2	0.2	6.7	1.2	0.64	352
1998 May 14–15	1998.366	0.02	16.8	...	16.4	0.1	2.3	0.4	0.48	1653
1998 Jul 3–5	1998.505	0.12	16.7	...	16.0	0.1	3.4	0.7	0.34	1643
1998 Aug 4–6	1998.59	0.02	17.2	...	16.3	0.1	2.5	0.5	0.66	1624
1998 Oct 9,11	1998.771	0.06	16.6	...	15.7	0.1	4.5	0.7	0.44	2952
1999 May 2–4	1999.333	0.06	17.2	...	16.2	0.2	2.7	0.5	0.82	2949
1999 Jul 24–25	1999.559	0.02	17.5	...	15.9	0.1	3.8	0.6	0.88	1527
2000 Apr 21	2000.305	0.14	15.7	S0-16
2000 May 19–20	2000.381	0.02	17.6	S0-16
2000 Jul 19–20	2000.548	0.14	17.3	S0-16
2000 Oct 18	2000.797	0.12	16.4	S0-16
2001 May 7–9	2001.351	0.08	17.1	...	16.6	0.1	2.0	0.3	0.81	1443
2001 Jul 28–29	2001.572	0.02	17.4	...	15.8	0.1	4.0	0.6	0.96	1702
2002 Apr 23–24	2002.309	0.06	17.4	S0-2
2002 May 23–24	2002.391	0.02	17.8	S0-2
2002 Jul 19–20	2002.547	0.22	16.9	S0-2
2003 Apr 21–22	2003.303	0.04	16.3	S0-38
2003 Jul 22–23	2003.554	0.08	16.7
2003 Sep 7–8	2003.682	0.18	17.0
2004 Apr 29–30	2004.327	0.02	16.6	...	16.2	0.1	2.8	0.6	0.21	1578
2004 Jul 25–26	2004.564	0.04	17.5	...	16.7	0.2	1.9	0.4	0.75	1572

Table 2
(Continued)

Date(UT)	Date (Epoch)	Bootstrap Fraction Cut ^a	Source Detection Limit ^b (mag)	Source Confusion with Sgr A*	K (mag)	K Error (mag)	Dereddened Flux (mJy)	Dereddened Flux Error (mJy)	Fraction of Bootstraps Detected	ΔT^c (minutes)
2004 Aug 29	2004.66	0.06	16.8
2005 Apr 24–25	2005.312	0.06	16.9	...	16.0	0.1	3.2	0.5	0.95	1633
2005 Jul 26–27	2005.566	0.16	16.9	...	15.8	0.1	4.0	0.6	0.66	1654

Notes.

^a Bootstrap fraction cut of a real source detection in each epoch is obtained at which the probability of a false detection within within 10 mas radius is always <1%.

^b Sgr A* detection limit is the 95th percentile of all K magnitudes in the sample which includes all sources with a bootstrap fraction higher than the bootstrap fraction cut in the central $2'' \times 2''$ FoV.

^c Time duration of the observations that contributes to the final speckle image for Sgr A* detections.

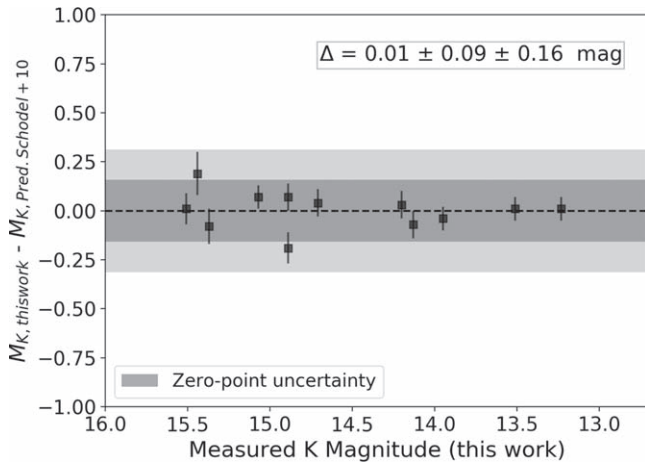


Figure 3. Difference between our measured K magnitude (from photometric system calibration) and the predicted K magnitude (bandpass corrected from Schödel et al. (2010) K_s) for calibrators used in Witzel et al. (2012). The measured K magnitudes are consistent with the predicted ones, with an average difference of 0.01 ± 0.09 mag and a zero-point uncertainty $\bar{\sigma}_{zp}$ of 0.16 mag (dark band; light band: $2\bar{\sigma}_{zp}$). This verifies that the early infrared (IR) measurements made based on speckle images are on the same photometric system as the later IR measurements obtained from AO.

3.3. Photometric Calibration

The list of extracted sources from speckle holography images is photometrically calibrated using a two-step procedure described in detail in Appendix A. This process results in an average photometric systematic zero-point uncertainty of 0.14 mag and an average relative photometric uncertainty of 0.04 mag respectively in NIRC K bandpass (see Table 1). While we use the standard photometry in Blum et al. (1996) as the initial system calibration, we find that our photometry of stars in the GC is consistent with both the photometric systems of Witzel et al. (2012) and Schödel et al. (2010) for the AO measurements of Sgr A* obtained between 2004 and 2017. The overall photometric difference between Schödel et al. (2010) and us is $\sim 1\%$ with an average difference of only 0.01 ± 0.09 mag and a zero-point uncertainty of 0.16 mag. See Figure 3.

3.4. Comparison of Speckle Holography Implementation

This work has introduced an improved implementation of speckle holography. Appendix B.2 compares in detail the performances between the current and the old versions and shows the clear improvements of version 2_2. In particular, version 2_2 is 0.4 mag deeper on average but can be as much as a factor of three more sensitive in the extreme. From here on, we only consider the analysis based on the new speckle holography (version 2_2), which has an average detection limit of 16.9 mag (see Table 1).

3.5. Identification of Sgr A* from Source List

We use the following steps to identify Sgr A* in the source list.¹³

1. Determine the position of Sgr A* in each epoch from the offsets between Sgr A* and IRS 16C and S0-2 because they are bright enough (IRS 16C: $K = 9.8$ mag; S0-2:

¹³ Here we use the source list excluding the most likely artifact sources identified in Appendix B.1.

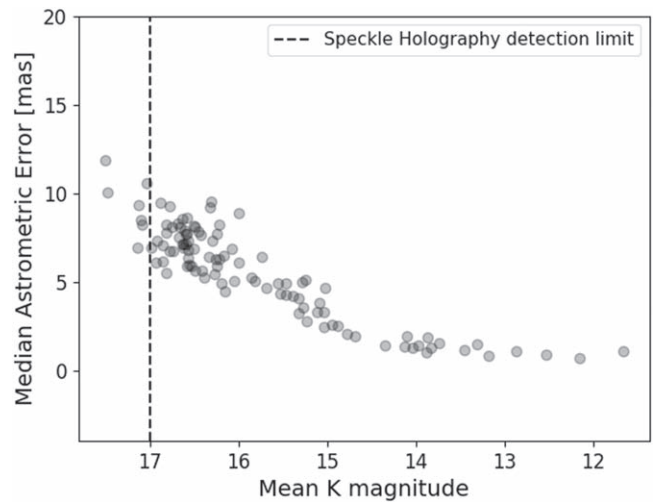


Figure 4. Astrometric uncertainty as a function of source brightness. While the brightest sources have an astrometric uncertainty of 1 mas, at the average speckle holography detection limit of $K \sim 17$ mag, shown as the dashed line, the astrometric uncertainty is typically 10 mas.

$K = 14.2$ mag) to always be identified and obtain the accurate positions in the image. The offsets were generated by aligning all of our speckle holography and AO data sets together. See Ghez et al. (2008), Gautam et al. (2019), Jia et al. (2019), and Sakai et al. (2019) for more details.

2. Search Sgr A* in the source list using the expected positions estimated in step (1). Sgr A* detected candidates are extracted if they are within the search radius of 10 mas. The search radius was determined by exploring the median astrometric error for all real detections in speckle epochs (Appendix B.1) in the central $2'' \times 2''$ region. See Figure 4. Empirically for sources with $K \sim 17$ mag (average speckle holography detection limit for all epochs, see Appendix B.2), the astrometric uncertainty is typically 10 mas. Based on this, we do not expect any real Sgr A* detections beyond 10 mas search radius.
3. Identify epochs where there is confusion with a known star that is passing within a 40 mas radius (Jia et al. 2019) away from Sgr A*.

4. Results

4.1. Sgr A* Detections

Results on the detections of Sgr A* in our 27 epochs of speckle holography imaging data fall into four categories: detections without source confusion (13); non-detections (5); confusion with brighter sources (8); and confusion with fainter sources (1). See Table 2 for details.

4.1.1. Detections without Source Confusion

Figure 5 presents the images of epochs with Sgr A* detections that are free from source confusion. The average observed magnitude of Sgr A* as obtained from these 13 epochs, which span the 7 yr period from 1998 to 2005, is $K = 16.0 \pm 0.4$ (standard deviation, std) with average relative photometric uncertainty of 0.1 mag, corresponding to the

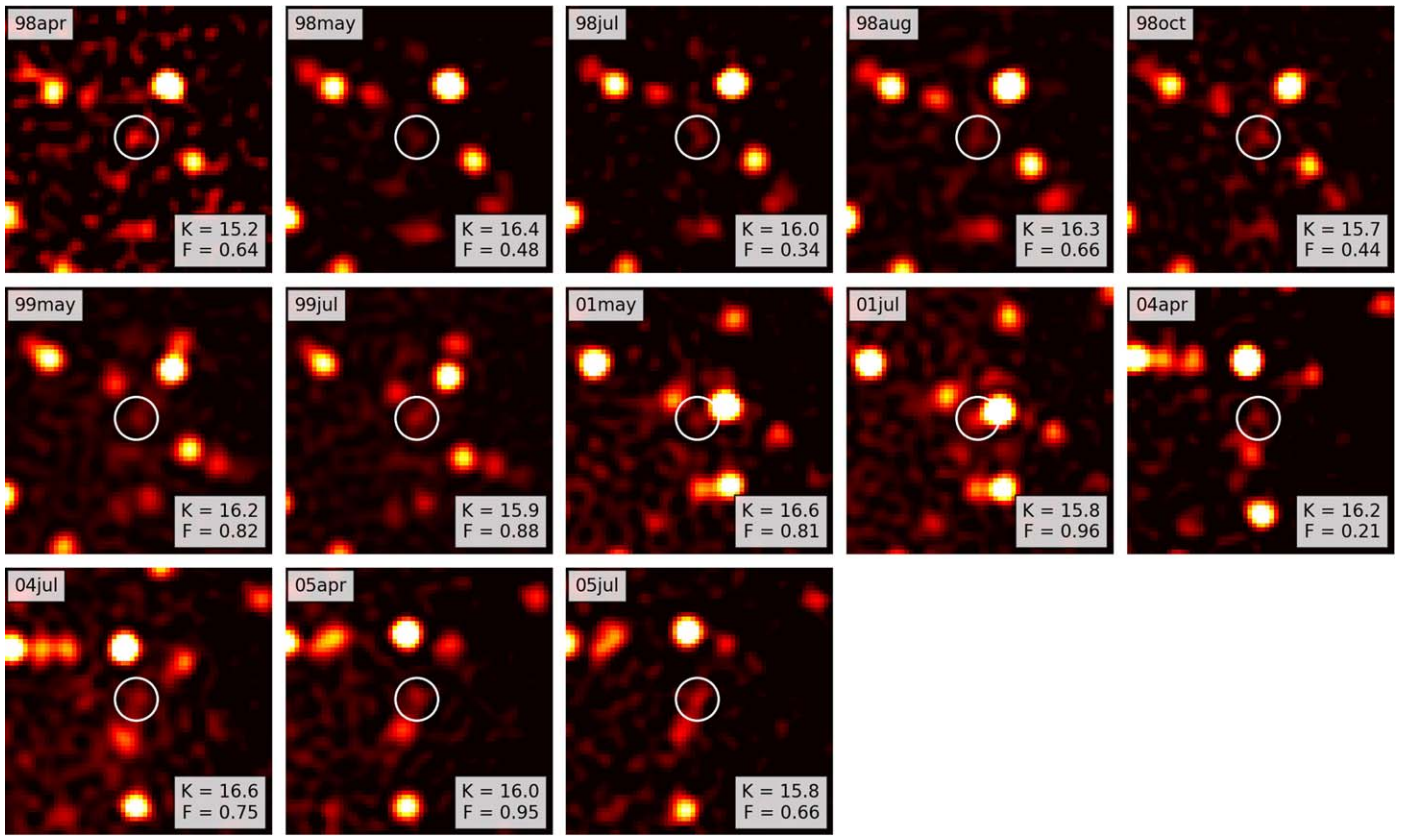


Figure 5. Speckle holography images with new Sgr A* detections (white circles). For each detection, the K magnitude (K) and the bootstrap fraction (F) are provided. These are the first IR detections of Sgr A* in the late 1990s and early 2000s.

average observed flux density of 0.35 ± 0.13 mJy with average relative photometric uncertainty of 0.04 mJy.

4.1.2. Non-detections

Among the 18 available epochs without source confusion (see Section 3.5), Sgr A* is not detected in five epochs. The brightness limit for Sgr A* in these epochs was determined by the source detection limit of that epoch (defined in Appendix B.1) and has values ranging from 16.0 to 17.0 mag.

4.1.3. Detections Confused with Brighter Sources

In eight epochs, Sgr A* was confused with a source brighter than its average value. As shown in Figure 6 confusion occurred with the following brighter stars: S0-2, $K_{\text{ave}} = 13.6$ mag in 2002 April, May, and July; S0-19, $K_{\text{ave}} = 15.0$ mag in 1995 June; S0-16, $K_{\text{ave}} = 15.1$ mag in 2000 April, May, July, and October. These epochs were removed from further analysis.

4.1.4. Detections Confused with Fainter Sources

In one epoch, Sgr A* was confused with a source fainter than its average value (see Figure 6). In 2003 April, there is a source detection that is the combination of Sgr A* ($K_{\text{ave}} = 16.0$ mag) and S0-38 ($K_{\text{ave}} = 16.5$ mag). Because the confusing source is fainter, the constraints on Sgr A* can be obtained from the photometry ($K = 16.4$ mag) and the astrometry ($K = 16.7$ mag). These are comparable to the detection limit of this image ($K = 16.3$ mag). We therefore place a limit on Sgr A* in this epoch of 16.3 mag.

4.2. Sgr A* Brightness (1996–2005)

4.2.1. Average Brightness

Figure 7 shows all our detections and detection limits of Sgr A* from 1996 to 2005. We convert the observed values into dereddened flux densities using the relationship $F_{K_s} = 6.67 \times 10^5 \times 10.0^{-0.4 \times (K_s - A_{\text{ext}, K_s})}$ mJy (Tokunaga 2000) and assuming $A_{\text{ext}, K_s} = 2.46$ mag extinction (Schödel et al. 2010, 2011). Then we use the filter transformation $F_K = 1.29 F_{K_s}$, which is computed for the observed color of Sgr A* ($H-K = 2.6$ mag), to convert from K_s fluxes to K fluxes (see Table 3). See Appendix A.1 for more discussion of the filter transformations. Here, in order to present the absolute dereddened fluxes all uncertainties contain both the photometric systematic uncertainties and relative uncertainties (see Appendix A). The average detected dereddened flux density (ignore the brightness limit) is 3.4 ± 1.2 mJy (standard deviation) with average uncertainty of 0.6 mJy (0.4 mJy of relative photometric uncertainty only). If including the brightness limit, (a) treat brightness limit as a value: the upper limit of the dereddened flux density is 2.9 mJy; (b) treat brightness limit as zero: the lower limit is 2.3 mJy. The average from detections and the variance (see following Section 4.2.2) are consistent with the expectations from simulations based on more recent AO observations (2006–2017) as modeled from Witzel et al. (2018; see Section 5.2.2, and Figures 13 and 14).

4.2.2. Long Timescale Variance (40 days–7 yr)

We used the first-order structure function to characterize the variability of Sgr A* over the 7 yr. This approach is similar to

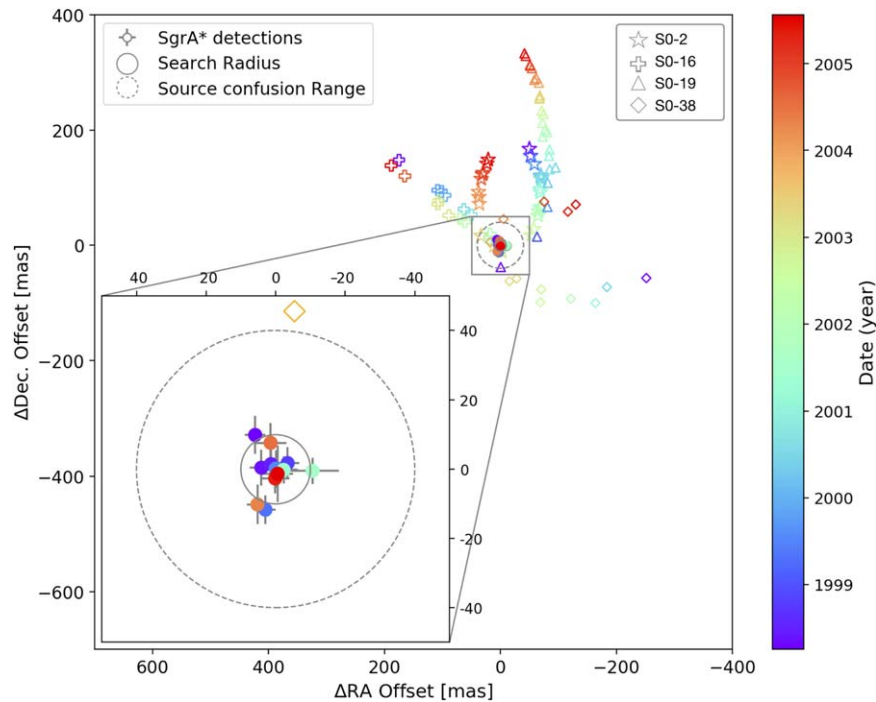


Figure 6. R.A. and decl. offsets of Sgr A* detections (points with errorbars) and of nearby star detections (symbols marked with names) relative to the predicted position of Sgr A* ((0, 0)). Different colors show the corresponding epochs. The inset panel zooms into the central part of the region. The gray solid circle marks the search radius of 10 mas (see Section 3.5) used to extract Sgr A* from the source list. The gray dashed circle shows the source confusion region (radius of 40 mas) within which nearby stars would cause bias and misdetection. We have removed confused Sgr A* detections and all nearby stars within this region in the inset panel. Overall, 13 detections of Sgr A* are free of source bias and used in this study.

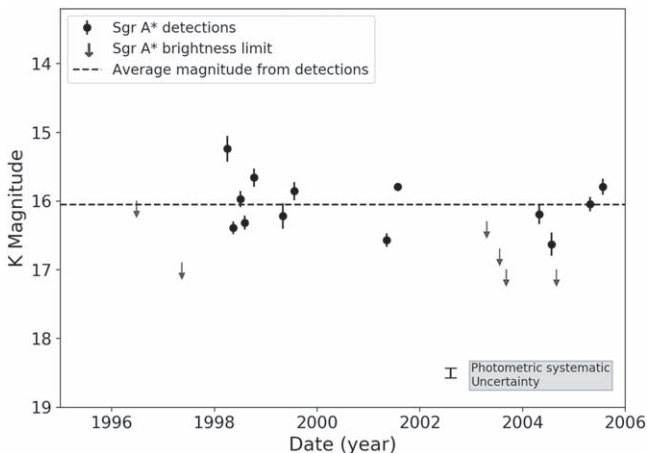


Figure 7. Light curve of Sgr A* from 1998 to 2005. The points with errorbars are the confirmed detections of Sgr A*. The arrows mark the brightness limit of Sgr A* in other non-detected epochs. The errorbar on the right bottom shows the average photometric systematic uncertainty of 0.14 mag. The average magnitude from the 13 detections is 16.0 mag.

Table 3
Filter Transformation for Sgr A*

Name	$K'_{\text{NIRC2}} - K_{\text{NIRC}}$	$K_{s,\text{NACO}} - K_{\text{NIRC}}$
Sgr A*	$0.367^{+0.01}_{-0.02}$	$0.275^{+0.01}_{-0.02}$

the analysis of the timescale and the intrinsic variability of active galactic nucleus (AGN) light curves (e.g., Simonetti et al. 1985; Hughes et al. 1992; Paltani 1999) and Sgr A* short time variability (e.g., Do et al. 2009; Witzel et al. 2012, 2018).

For the set of flux measurements shown in the light curve, $s(t)$, the first-order structure function $V(\tau)$ measures the flux density variance for a given time separation τ :

$$V(\tau) \equiv \langle [s(t + \tau) - s(t)]^2 \rangle. \quad (2)$$

We calculated $[s(t + \tau) - s(t)]^2$ using Sgr A* dereddened fluxes reported in this work for all possible pairs of time lags from real speckle observational time series. Then we put the variances into bins with a bin size of 100,000 minutes (~ 70 days). This yields nine bins covering the timescale between 42 days and 7.3 yr, and each bin contains at least five and as many as 19 data points. In each bin, we assigned the median lag time to be the lag time for that bin, and the average of the $V(\tau)$ values to be the value of the structure function at that lag. The error of the structure function for each bin is calculated from $\sigma_{\text{bin}} / \sqrt{N_{\text{bin}}}$. Here σ is the standard deviation of the $V(\tau)$ values and N is the number of points in that bin. The structure functions calculated with Sgr A* dereddened fluxes from observations are presented in Figure 8. The structure function is flat over timescale from 42 days to 7.3 yr, and has an average value of 3.1 mJy^2 with the standard deviation of 1.1 mJy^2 .

5. Discussion

5.1. Impact of G1 Passage

Based on 7 yr of speckle holography data, we can use the variability of Sgr A* as the indication of the accretion activity between 1998 and 2005. During this time, the dusty source G1 went through the closest approach in 2001. This object has similar observational properties to G2, which is the first example of a spatially resolved object tidally interacting with Sgr A*.

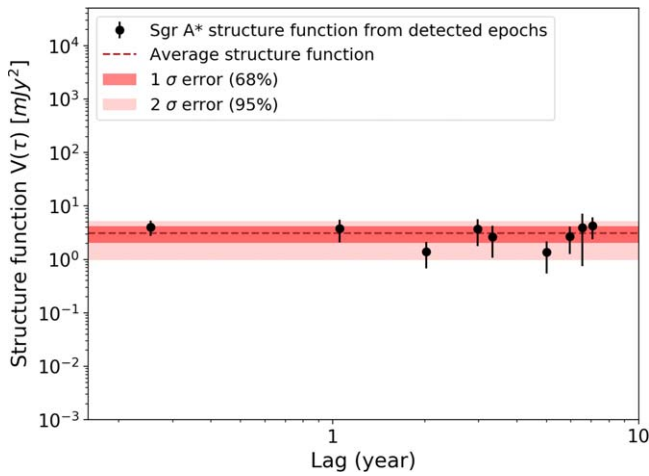


Figure 8. Sgr A* structure function $V(\tau)$. The average structure function from 13 detections is $3.1 \pm 0.3 \text{ mJy}^2$ (red band).

hypotheses for the nature of G1 are similar to those proposed to explain G2. These predictions range from compact gas clouds to the product of binary mergers (Gillesen et al. 2012; Murray-Clay & Loeb 2012; Phifer et al. 2013). Predictions of compact gas clouds near Sgr A* suggest that they may increase the accretion flow onto Sgr A*. For G2, one prediction (Schartmann et al. 2012) is that if it is a gas cloud, it may be tidally disrupted and accrete onto Sgr A*, increasing the black hole’s luminosity by up to a factor of 80. Because G1’s tidal radius is even smaller than that of G2, it would be more influenced by the black hole. If G1 was a gas cloud and some of the gas had been accreted onto the black hole, we may expect the additional accretion at the periape. We marked the time following of G1’s periape passage in Figure 9. Between 2001 and 2005, there is no increase in flux observed in Sgr A*. Sgr A* was quite steady with no evidence of large variations in brightness. The result is consistent with G1 being a self-gravitating object (such as a merger of two stars) as suggested by Witzel et al. (2017).

5.2. Long Timescale Variability of Sgr A*-IR

While the short-term variability of Sgr A* in the NIR is well characterized as a red-noise process, the long timescale variation has not been well probed. In order to explore if the observed long timescale variability shown in this work is consistent with models derived from shorter timescales, we simulate the NIR Sgr A* light curves with the model presented in Witzel et al. (2018; see Section 5.2.1). Section 5.2.2 presents the comparison of the simulations to the observations. See Section 5.2.3 for further discussion of the characteristic break timescale.

5.2.1. Light Curve Simulations

This model contains two key components. The first component describes the temporal characteristics using the PSD, which is modeled as a broken power law

$$\text{PSD}(f) \propto \begin{cases} f^{-\gamma_0} & \text{for } f < f_b \\ f^{-\gamma_1} & \text{for } f \geq f_b, \end{cases} \quad (3)$$

where $\gamma_0 = 0$ (assumed), $\gamma_1 = 2.1 \pm 0.1$, $f_b = (4.1 \pm 0.7) * 10^{-3} \text{ minute}^{-1}$ (which corresponds to a timescale of $\tau \sim 245$ minutes). See Figure 10 for the modeled PSD.

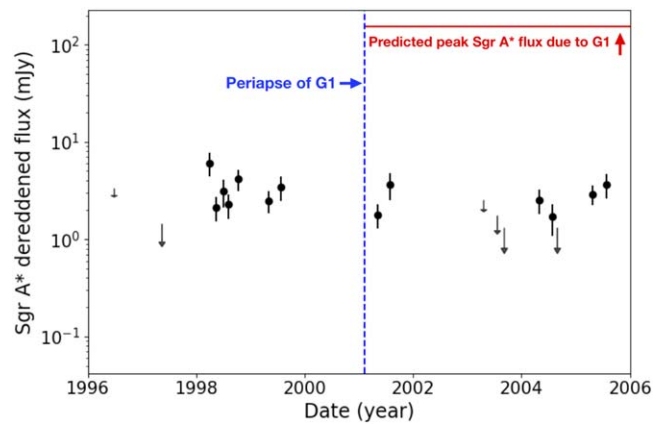


Figure 9. Impact of G1’s closest approach on the brightness of Sgr A*. The blue dashed line marks the G1’s periape (2001), and red line marks the predicted peak Sgr A* flux due to the closest approach of G1. No brightening or flares of Sgr A*, i.e., no apparent impacts of G1 on the Sgr A* IR emission, were observed between 2001 and 2005.

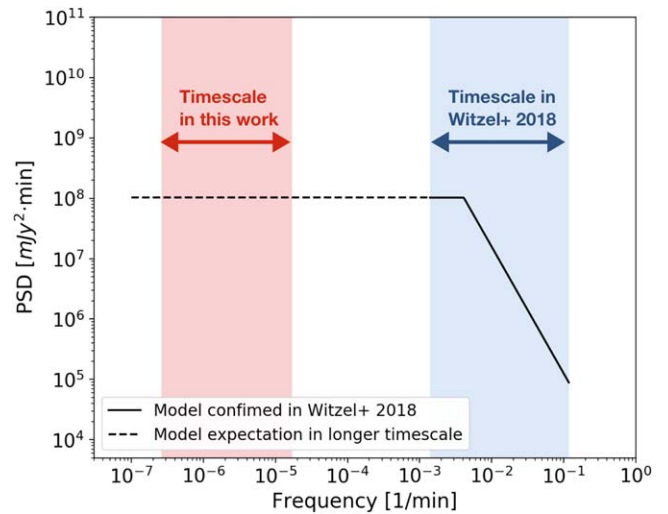


Figure 10. Modeled PSD of Sgr A* presented in Witzel et al. (2018). The solid line shows the broken power-law PSD that has been confirmed in previous short-term variability observations with a break timescale of $\tau \sim 245$ minutes. The dashed line shows the assumed flat PSD in a longer timescale. The blue band marks the timescale probed in existed studies, and the red band marks the timescale that we explored in this work.

The second component describes the distribution of fluxes with a log-normal probability density function (PDF)

$$\mathcal{P}[F | (\mu_{\log n}, \sigma_{\log n})] = (\sqrt{2\pi} F \sigma_{\log n})^{-1} \cdot \exp \left(-\frac{\left[\ln \left(\frac{F(K)}{\text{mJy}} \right) - \mu_{\log n} \right]^2}{2 \sigma_{\log n}^2} \right), \quad (4)$$

where Sgr A* flux density $F \in [0, \infty]$, log-normal mean in K -band $\mu_{\log n} \in [-\infty, +\infty]$, and log-normal standard deviation in K -band $\sigma_{\log n} \in [0, \infty]$.

Following the method in Timmer & Koenig (1995) and using the modeled parameters in Witzel et al. (2018), we are able to generate the simulated light curves of Sgr A* using the same time series sampling as the real observations following the time of

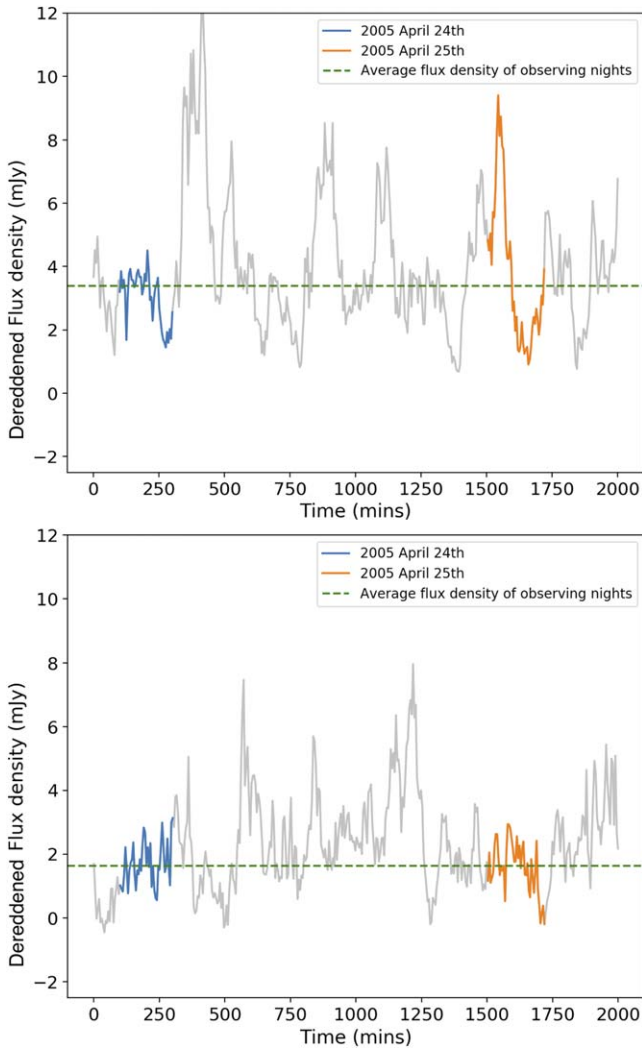


Figure 11. Two examples of the simulated Sgr A* light curve (gray curve) over the two real observing nights in 2005 April (blue and orange parts, respectively). The simulated light curves were generated following the modeled PSD and a log-normal flux distribution, and using the same time series sampling as the real observations (see Section 5.2). The horizontal line shows the average flux density from the two observing nights (blue and orange), which imitates the final combined image.

datacubes. Here we assigned the time of each datacube to be the time of first frame in that cube. We have tested the effects of only using the datacube time series instead of frame time series if considering time delay between each frame. No significant differences were found. We therefore use the datacube sampling for computational efficiency. To create each simulated light curve (with observed flux density), we added Gaussian-distributed noise ($\sigma = 0.035$ mJy, average uncertainty from speckle observations; see Section 4.1.1). In order to convert from observed fluxes at Kp (NIRC2 AO instrument used in this model from Witzel et al. 2018) to our observations at K (NIRC speckle instrument), we did filter transformation for Sgr A* of NIRC2 Kp–NIRC K = $0.367 \text{ mag}^{+0.01}_{-0.02}$ (see Table 3), similar to the bandpass correction described in Section 4.2.1 and Appendix A.1. As a final step, the dereddened flux of a simulated light curve was obtained following the process presented in Section 4.2.1. See Figure 11 for the examples of the final simulated light curve with dereddened flux.

5.2.2. Comparison of the Simulations to the Observations

We extracted the average flux density of every single simulated light curve (see Section 5.2.1), in order to imitate each real observational image that combines and averages the fluxes from all datacubes. For each epoch, we repeated the simulation 10,000 times using the posterior values from Witzel et al. (2018). See Figure 12 for the distribution of the average dereddened flux density of simulated light curves in 19 available epochs,¹⁴ and Sgr A* observations for comparison.

Then we used simulated Sgr A* light curves to calculate the expectation of Sgr A* average flux and average structure function of our available epochs based on the model described above. In order to take into account the effect of detection limit of observations in simulations, we calculate the expectation of Sgr A* average flux and average structure function only with the simulated fluxes that are higher than the detection limit in that epoch. The steps are as follows.

1. Probe 19 available epochs that have either a detection or a detection limit.
2. Among all 10,000 simulations, for each one set of simulated flux densities from all 19 epochs, mark the epoch if the simulated flux density passes the corresponding Sgr A* detection limit. Calculate one average flux density and one series of structure functions (for all possible pairs of time lags) with only marked epochs. Then generate one Sgr A* average variance.
3. Repeat step (2) for all 10,000 sets of simulations. The number of epochs used to generate each average flux density and series of structure functions varies depending on how many simulated flux densities pass the detection limit in that round.

Figure 13 presents the comparison of Sgr A* average dereddened flux from 13 detected epochs and its expectation calculated above from simulations based on the model in Witzel et al. (2018). Figure 14 presents average structure function of Sgr A* detections and its expectation from simulations. The observed Sgr A* average flux density and average structure function are consistent with the predictions that are modeled from Witzel et al. (2018) with a power-law PSD and log-normal flux distribution. These results show that Sgr A* long-term variability status in the past (1998–2005) is well consistent with the extrapolation from shorter timescale AO-based observations at later time. Sgr A* has had similar brightness and variability characteristics over two decades.

5.2.3. Characteristic Break Timescale

In this work, the flat structure function of Sgr A* calculated from observations indicates that there is no need for a second PSD break in the longer timescale that we investigated here. Any significant increase of power in the PSD between ~ 80 days and 7 yr can be excluded. Previous studies of timescales from minutes to hours presented a break timescale in the NIR PSD of Sgr A* (Eckart et al. 2006; Meyer et al. 2008, 2009; Do et al. 2009) and the latest analysis (Witzel et al. 2018) reports a correlation timescale of ~ 245 minutes. Our result is consistent with the assumption of a zero-slope PSD after the correlation timescale based on the model from Witzel et al. (2018). Therefore, the 245 minute timescale remains the only

¹⁴ With either a detection or a detection limit.

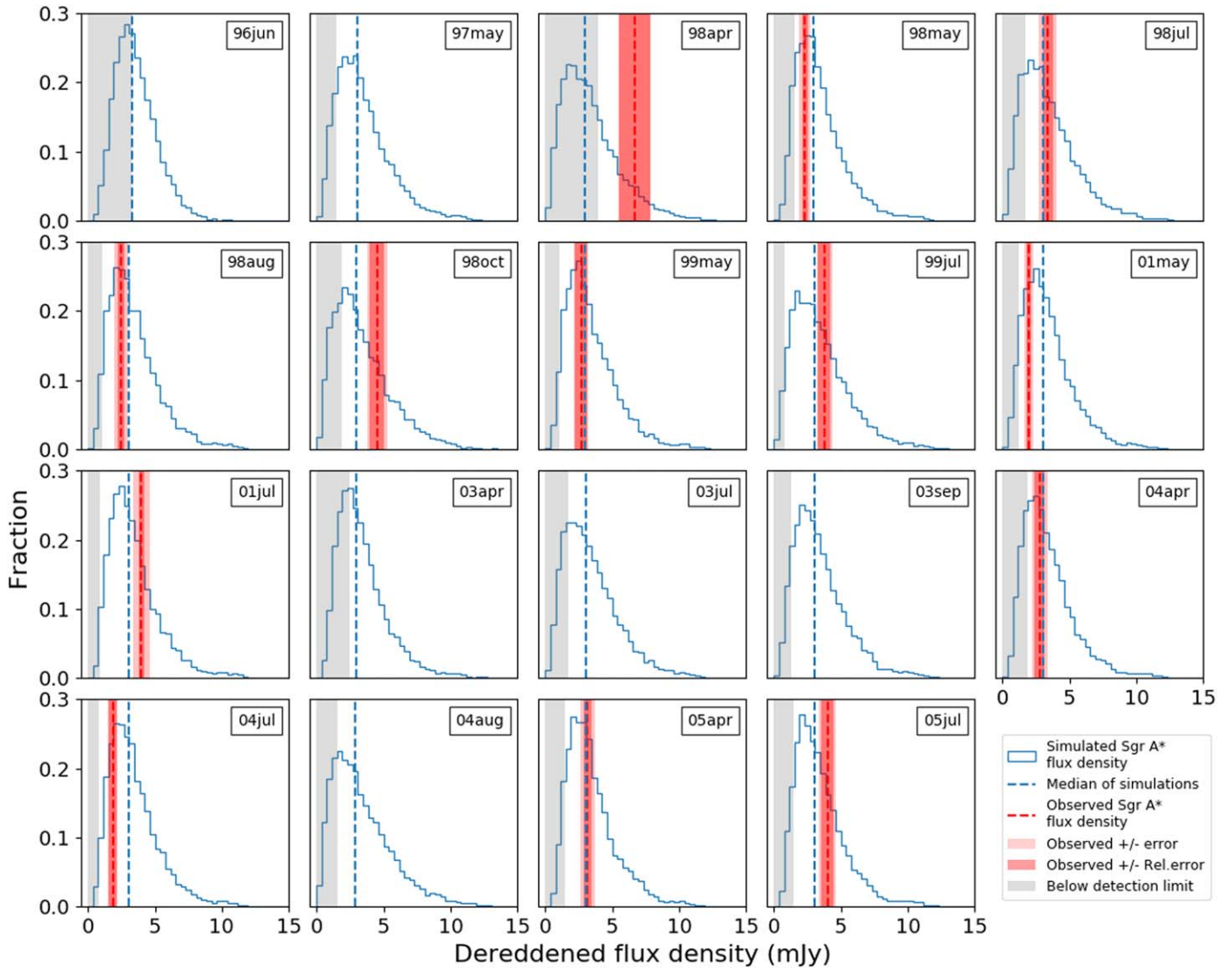


Figure 12. Distribution of average flux densities of 10,000 simulated light curves (Section 5.2.1) compared to the observations of Sgr A*. We probed 19 available epochs with either a detection or a detection limit. The blue curve presents the histogram of 10,000 average flux densities with the median shown as a blue dashed line. The red dashed line with bands marks the observed Sgr A* dereddened flux density with errors (light: total photometric error; dark: relative photometric error only; see Appendix A). The gray shaded region in each epoch presents the fluxes lower than the detection limit (defined in Appendix B.1).

confirmed break timescale in the NIR PSD of Sgr A*. Beyond this break timescale, Sgr A* appears to be uncorrelated with time, and the amplitude of the variations stop increasing.

The speckle era of Keck (1995–2005) that we have explored in this work overlaps with some AO data sets between 2002 and 2005 (VLT NAOS/CONICA 2002–2005; Keck NIRC2 2004–2005). The results of overlapping AO data sets do not show any significant deviations from the average flux obtained with speckle data sets in the same period. Witzel et al. (2018) has summarized and reported the analysis based on AO data sets (VLT NAOS/CONICA 2003–2010; Keck NIRC2 2004–2016). The results obtained from AO measurements appear to be consistent with the speckle results reported in this work.

The characteristic timescale of the X-ray variability of AGNs and black hole X-ray binaries (BHXRBs) has been similarly investigated (see, e.g., Uttley et al. 2002; Markowitz et al. 2003; Uttley & McHardy 2005). Previous studies hypothesized that the characteristic break timescales (the break frequency, observed in BHXRBs) of AGNs scale linearly with the mass of

black holes with a correction factor of bolometric luminosity of the accretion flow (McHardy et al. 2006). This led to the conclusion that AGNs are scaled-up galactic black holes. Therefore, the variability of the SMBH at the GC, Sgr A*, serves well as the most under-luminous black hole system to test the scaling relationship of AGNs (Meyer et al. 2009; Witzel et al. 2018).

6. Conclusions

The long-term variability of the SMBH at the GC, Sgr A*, has been studied with the analysis of speckle data (1995–2005) obtained from the W. M. Keck 10 m telescope. The application of the speckle holography technique enables us to investigate Sgr A* with deeper detections than in any previous work. This study presents the first NIR detection of Sgr A* prior to 2002. We are able to monitor the long-term variability of Sgr A* in the NIR with a time baseline of 7 yr with analysis for astrometry and photometry of Sgr A*. We present a Sgr A* light curve from

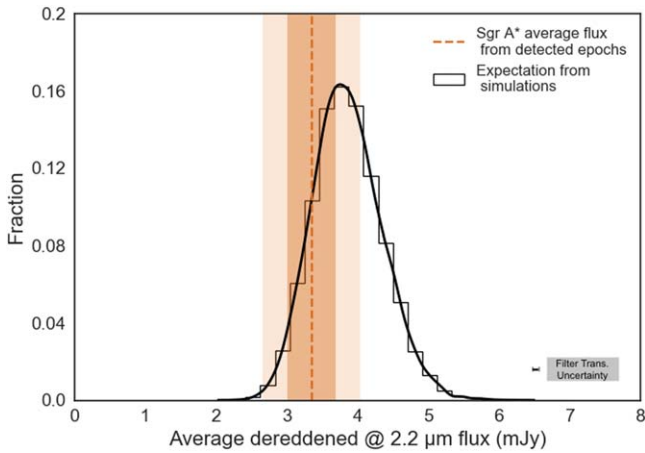


Figure 13. Sgr A* average flux from early observations (1996–2005) and its expectation from simulations based on more recent observations (2006–2017). The orange line with band marks the average dereddened flux calculated from 13 detected epochs with errors (dark: $\sigma/\sqrt{N_{\text{detections}}}$; light: $2\sigma/\sqrt{N_{\text{detections}}}$). The histogram with corresponding kernel density estimation presents the distribution of expected average flux density from simulations based on the model in Witzel et al. (2018). The errorbar on the bottom right shows the filter transformation uncertainty of 0.04 mJy. Sgr A* has had similar brightness over two decades.

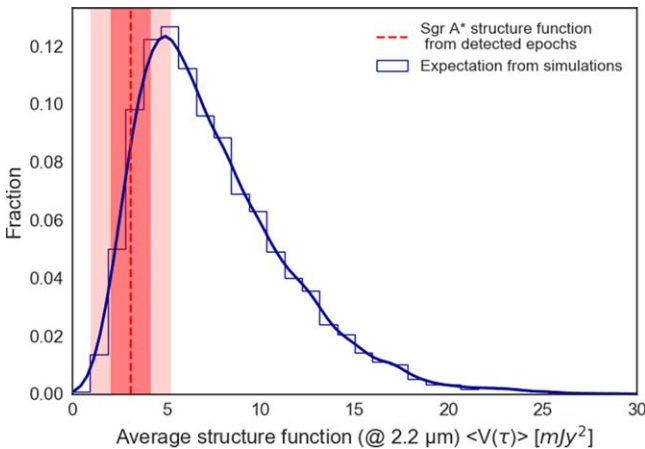


Figure 14. Sgr A* average structure function $V(\tau)$ from observations and its expectation from simulations. The red line with the band marks the average structure function calculated from 13 detected epochs with 1σ error and 2σ error, respectively (see the red points in Figure 8). The blue histogram with corresponding kernel density estimation presents the distribution of expected average structure function from simulations based on the model in Witzel et al. (2018; see the red bands in Figure 8). Sgr A* has had similar variability characteristics over two decades.

1998 to 2005, indicating that Sgr A* was stable and showed no extraordinary flux excursions during this time. The average observed magnitude of Sgr A* as obtained from the last 7 yr (1998–2005) of speckle holography data sets is $K = 16.0 \pm 0.4$ with average relative photometric uncertainty of 0.1 mag, corresponding to the average observed flux density of 0.35 ± 0.13 mJy with average uncertainty of 0.04 mJy. The average dereddened flux density is 3.4 ± 1.2 mJy with a total average photometric uncertainty of 0.6 mJy. The results agree very well with the average observed AO measurements of $K = 16.1 \pm 0.3$ (2005–2017), and are consistent with the extrapolation modeled from AO-based shorter timescale studies. Sgr A* is quite stable without significant change in this time baseline of 7 yr based on the structure function timing analysis, which indicates that 245 minutes still remains the dominant

break timescale. Based on the results, the periaapse passage of the object G1 did not result in any measurable change of the mean accretion rate onto Sgr A*.

The primary support for this work was provided by NSF, through grant AST-1412615, and UCLA, through faculty salaries. Additional support was received from the Heising-Simons Foundation, the Levine-Leichtman Family Foundation, the Preston Family Graduate Fellowship (held by B.N.S and A.G.), UCLA Galactic Center Star Society, UCLA *Cross-disciplinary Scholars in Science and Technology* (CSST) Fellowship, NSF *Research Experiences for Undergraduates* (REU) grant No. PHY-1460055, and the European Union’s Seventh Framework Programme (FP7/2007-2013)/ERC grant agreement No. [614922] (R.S.). This research was based on data products from the Galactic Center Orbit Initiative (GCOI), which is hosted at UCLA and which is a key science program of the Galactic Center Collaboration (GCC). These data products were derived from data originally obtained from W. M. Keck Observatory. The W. M. Keck Observatory is operated as a scientific partnership among the California Institute of Technology, the University of California, and the National Aeronautics and Space Administration. The authors wish to recognize that the summit of Maunakea has always held a very significant cultural role for the indigenous Hawaiian community. We are most fortunate to have the opportunity to observe from this mountain. The Observatory was made possible by the generous financial support of the W. M. Keck Foundation.

Appendix A Photometry used in this Work

In order to obtain photometry for sources from the speckle holography images, we performed a two-step procedure. In the first step (Appendix A.1), the photometric systematic scale is established with an uncertainty of 0.14 mag (1σ). In the second step (Appendix A.2), we select a set of stable secondary photometric calibrators to improve the relative photometry to ± 0.04 mag (1σ).

A.1. Photometric System Calibration

We perform photometric system calibration using four initial calibration stars (IRS 16C, IRS 33E, S2-16 and S2-17). These stars are the only ones that have both reference flux measurements as reported by Blum et al. (1996) and are located within our FoV. As Figure 15 shows, IRS 16C is ideally located close to the center of the FoV and therefore measured in every epoch. S2-17 and S2-16 are measured in almost every epoch, and in each epoch typically have more than half of the frames obtained. In contrast, IRS 33E is much closer to the edge of the final FoV and detected in only two-thirds the epochs, and in these epochs it typically has one-third of the frames.

There are three considerations made to convert Blum’s measurements into flux predictions for the speckle holography measurements made with NIRC. First and most importantly, we applied an aperture correction to the Blum’s measurements to account for the low resolution of their measurements. With $\sim 1''$ seeing, Blum’s measurements include neighboring stars that are resolved in our speckle holography observations. Therefore, we did aperture correction by subtracting the fluxes

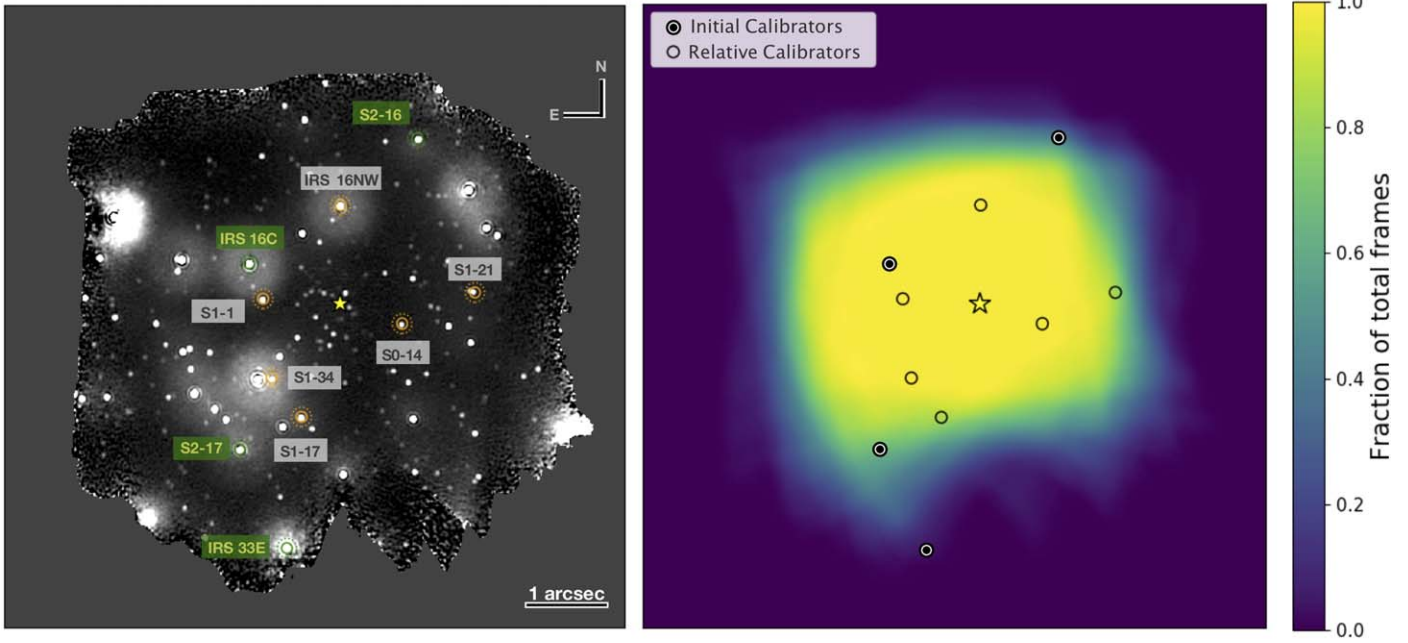


Figure 15. Location of photometric calibrators. Left panel: background is the speckle holography image from 2002 April observation. The four initial photometric calibrators used in photometric system calibration are marked with green circles. The six relative photometric calibrators are marked with orange circles. The yellow star symbol shows Sgr A*'s position. Right panel: the fraction of total frames used in each pixel for the final image from 2002 April observation. Filled circles show initial photometric calibrators, and the open circles show relative photometric calibrators. The relative calibrators are chosen to be isolated stars that uniformly cover the FoV with minimal edge effects.

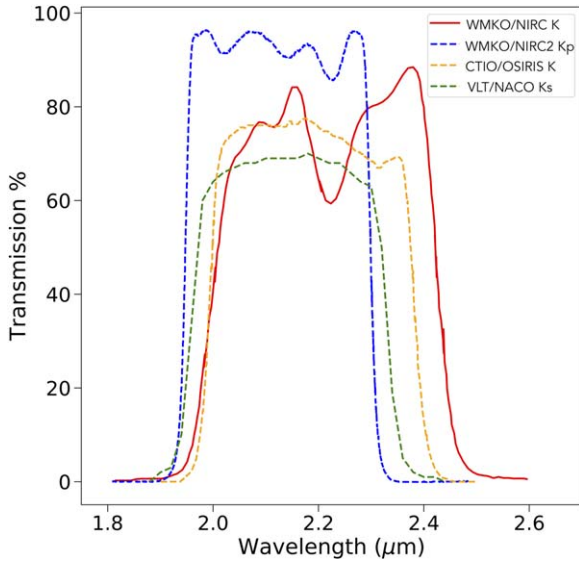


Figure 16. Comparison of the $2\ \mu\text{m}$ bandpass filter used in this work. The transmission curves for the WMKO/NIRC/K (this work), WMKO/NIRC2/Kp (Gautam et al. 2019), CTIO/OSIRIS/K (Blum et al. 1996), and VLT/NAKO/Ks (Schödel et al. 2010). Owing to the different transmissions, there are photometric offsets between the filters (see Appendix A.1).

of nearby sources within the radius of $\sim 0''.5$ aperture. The correction ranges from 0 to 0.3 mag. Second, owing to the slight differences between the bandpass used in Blum et al. (1996) and our NIRC K instrument (see Figure 16), there are photometric offsets between the filters. These offsets were calculated by convolving the extinguished stellar model atmospheres with the filter functions (see Appendix A in Gautam et al. 2019 for more details). The offsets range from 0.06 to

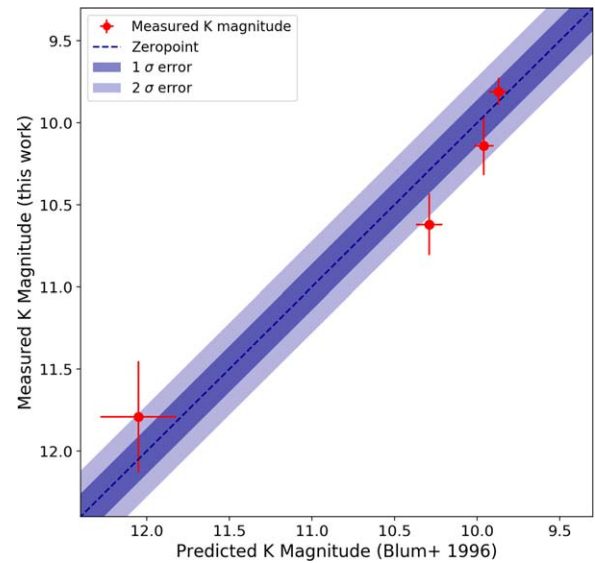


Figure 17. Comparison of our measured K magnitude (from photometric system calibration) to the predicted K magnitude (bandpass corrected from Blum et al. 1996) for all four initial calibrators (red points with errorbars). The resulting zero-point uncertainty is 0.14 mag (1σ).

0.11 mag. Third, the uncertainties in the predicted brightness of the four calibrators are increased by the known level of variability from the work in Gautam et al. (2019). The additional uncertainties range from less than 0.03–0.07 mag, which for each star is less than the uncertainty in the original Blum's measurements. Table 4 summarizes all these considerations and provides the final predictions.

The zero-point for each epoch, z_p , was calculated as a weighted mean of the ratios between the calibrators' measured

Table 4
Calibration Stars

Star Name	Calib. Type	N^a Epoch	Varia. ^b (mag)	$K_{\text{Blum}+96}$	Aperture Corr. ^c (δmag)	K_{NIRC}^- $K_{\text{Blum}+96}$	$K_{\text{NIRC,Pred.}}^d$	K_{NIRC} Init. ^e	K_{NIRC} Rel. ^f
IRS 16C	Phot.	27	0.040	9.86 ± 0.05	0.07 ± 0.001	-0.06 ± 0.01	$9.87 \pm 0.06^g \pm 0.04^h$	$9.81 \pm 0.04 \pm 0.14$	9.79 ± 0.08^i
IRS 33E	Phot.	18	<0.035	10.02 ± 0.05	0 ± 0	-0.06 ± 0.01	$9.96 \pm 0.06 \pm 0.04$	$10.14 \pm 0.04 \pm 0.14$	10.04 ± 0.07
S2-17	Phot.	26	<0.034	10.03 ± 0.07	0.32 ± 0.007	-0.06 ± 0.01	$10.29 \pm 0.09 \pm 0.04$	$10.62 \pm 0.04 \pm 0.14$	10.64 ± 0.06
S2-16	Phot.	25	0.070	11.90 ± 0.22	0.26 ± 0.001	-0.11 ± 0.01	$12.05 \pm 0.23 \pm 0.04$	$11.79 \pm 0.09 \pm 0.14$	11.79 ± 0.10
IRS 16NW	Rel.	27	<0.031	$10.00 \pm 0.04 \pm 0.14$	10.00 ± 0.05
S1-17	Rel.	26	<0.030	$12.24 \pm 0.04 \pm 0.14$	12.24 ± 0.04
S1-34	Rel.	26	<0.029	$12.92 \pm 0.04 \pm 0.14$	12.93 ± 0.04
S1-1	Rel.	27	<0.029	$12.85 \pm 0.04 \pm 0.14$	12.86 ± 0.04
S1-21	Rel.	25	<0.030	$13.26 \pm 0.05 \pm 0.14$	13.23 ± 0.05
S0-14	Rel. & Veri.	26	<0.028	$13.50 \pm 0.03 \pm 0.07$	$13.50 \pm 0.04 \pm 0.14$	13.51 ± 0.05
S0-13	Veri.	27	<0.030	$13.22 \pm 0.04 \pm 0.07$	$13.21 \pm 0.04 \pm 0.14$	13.23 ± 0.04
S0-6	Veri.	27	<0.030	$13.99 \pm 0.03 \pm 0.07$	$13.95 \pm 0.04 \pm 0.14$	13.95 ± 0.04
S0-12	Veri.	27	<0.034	$14.20 \pm 0.04 \pm 0.07$	$14.15 \pm 0.04 \pm 0.14$	14.13 ± 0.05
S0-4	Veri.	27	<0.032	$14.17 \pm 0.04 \pm 0.07$	$14.22 \pm 0.04 \pm 0.14$	14.20 ± 0.05
S1-10	Veri.	27	<0.029	$14.67 \pm 0.04 \pm 0.07$	$14.69 \pm 0.04 \pm 0.14$	14.71 ± 0.04
S0-31	Veri.	27	<0.037	$15.08 \pm 0.05 \pm 0.07$	$14.86 \pm 0.06 \pm 0.14$	14.89 ± 0.07
S1-33	Veri.	27	<0.030	$14.82 \pm 0.04 \pm 0.07$	$14.92 \pm 0.04 \pm 0.14$	14.89 ± 0.04
S0-11	Veri.	27	<0.035	$15.00 \pm 0.04 \pm 0.07$	$15.06 \pm 0.05 \pm 0.14$	15.07 ± 0.06
S1-6	Veri.	27	0.069	$15.25 \pm 0.08 \pm 0.07$	$15.35 \pm 0.08 \pm 0.14$	15.44 ± 0.08
S0-27	Veri.	26	0.049	$15.45 \pm 0.05 \pm 0.07$	$15.35 \pm 0.07 \pm 0.14$	15.37 ± 0.10
S1-31	Veri.	26	<0.036	$15.50 \pm 0.05 \pm 0.07$	$15.51 \pm 0.05 \pm 0.14$	15.51 ± 0.09

Notes.

^a Number of epochs detected in the speckle holography images.

^b Additional uncertainty from variability (Gautam et al. 2019), which for each star is less than the uncertainty of the original Blum's measurements. Reported in Gautam et al. (2019).

^c Aperture correction with a radius of $0''.5$ (see Appendix A.1).

^d Predicted NIRC K mag for four initial calibrators obtained from Blum et al. (1996) after aperture and bandpass correction; predicted NIRC K mag for 12 verification calibrators obtained from Schödel et al. (2010) after bandpass correction. See details in Appendix A.1.

^e Measured NIRC K magnitude after initial photometric system calibration (see Appendix A.1).

^f Measured NIRC K relative magnitude after relative photometric calibration (see Appendix A.2).

^g Photometric uncertainty with additional variability uncertainty.

^h Average photometric systematic zero-point uncertainty.

ⁱ Relative photometric uncertainty (see Appendix A.2). The average zero-point uncertainty for relative photometry is 0.04 mag.

References. Blum et al. (1996), Gautam et al. (2019).

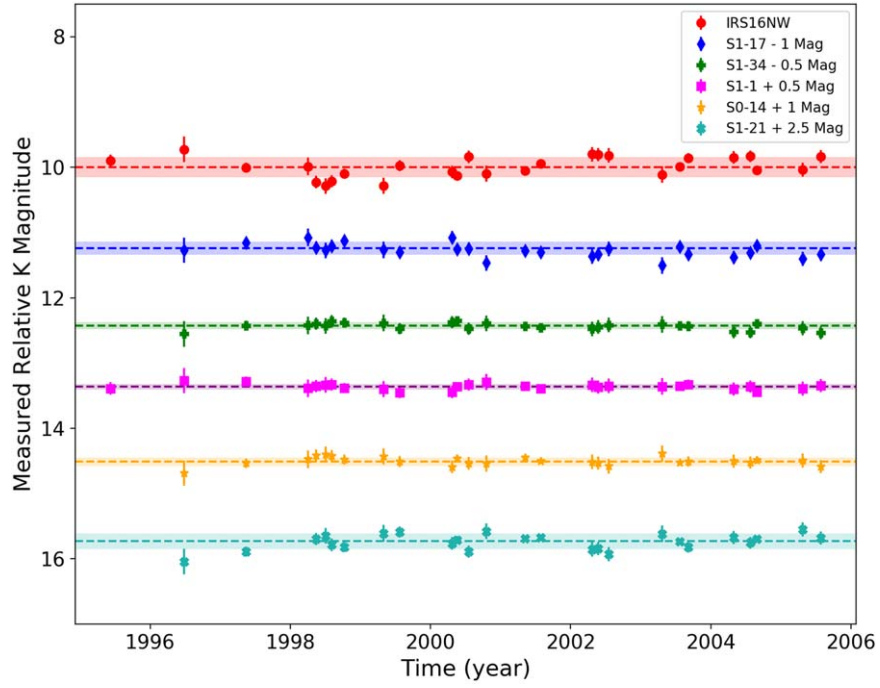


Figure 18. Light curve with measured relative K magnitude for each of the secondary calibrator star after relative photometric calibration. The line with band shows the weighted mean and the rms across all detected epochs. The relative photometry has an average uncertainty of 0.04 mag (1σ).

instrumental flux and reference flux ($d_i = f_{i,\text{reference}}/f_{i,\text{measured}}$):

$$z_p = \frac{\sum w_i * d_i}{\sum w_i}. \quad (5)$$

Here, w_i indicates the weight for calibrator i , derived from uncertainty in its reference flux ($\sigma_{f,i}$): $w_i = (\sigma_{f,i})^{-2}$. Zero-point uncertainties in the photometric calibration for each observation epoch, σ_{z_p} , were derived from the weighted standard deviation of flux differences (between the calibrator stars' reference magnitudes and measured magnitudes) then divided by $\sqrt{N_{\text{Calibs.}} - 1}$ (here $N_{\text{Sys,Calibs.}} = 4$).

$$\sigma_{z_p} = \sqrt{\frac{\sum w_i (d_i - z_p)^2}{\sum w_i}} / \sqrt{N_{\text{Calibs.}} - 1}. \quad (6)$$

Each epoch's zero-point uncertainty is reported in Table 1. Overall, we achieved an average zero-point uncertainty $\bar{\sigma}_{z_p}$ for the photometric system calibration of 0.14 mag in NIRC K bandpass (see Figure 17).

As a final step, we verify that our speckle holography measurements are at the same photometric system as Witzel et al. (2018), whose model is used to simulated the NIR Sgr A* light curves in Section 5.2. Witzel et al. (2012) used and reported 13 stars as photometric calibrators, 12 of which are contained in our studies (see Appendix B). These measurements were tied to the absolute K_s observations reported in Schödel et al. (2010). Therefore, we transformed from the VLT NACO K_s to NIRC K (see Figure 16 for different transmissions) with bandpass corrections that are similar to that process described above. Figure 3 shows that our measured K magnitudes (after photometric system calibration) are highly consistent with the predicted K

magnitudes (corrected from K_s photometric system), with an average difference of only 0.01 ± 0.09 mag (see Table 4).

A.2. Relative Photometric Calibration

We perform relative photometric calibration using the secondary calibrator stars identified by Gautam et al. (2019) that are detected in the FoV of our observations. These calibrator stars, IRS 16NW, S1-17, S1-34, S1-1, S0-14, and S1-21 (see the left panel of Figure 15), are selected to be non-variable and well-distributed in the FoV. The reference fluxes of these calibrators were obtained from the photometric system calibration described in Appendix A.1 (see Table 4). See Figure 18 for the light curve with measured relative K magnitude for each of the calibrator after relative photometric calibration. The derivation of the zero-point and uncertainties in the relative calibration is the same as for the photometric system calibration procedure (see Appendix A.1). We achieved an average uncertainty $\bar{\sigma}_{z_p}$ for the relative photometric calibration of 0.04 mag in the NIRC K bandpass. See Table 1 for the details of a single epoch.

Appendix B

Source Analyses for Speckle Holography

B.1. Bootstrap Fraction Threshold and Detection Limit

In order to define criteria for real detections, we can use the stellar photometric and astrometric information from the analysis of our extensive AO imaging data (e.g., Jia et al. 2019), which are on the order of three magnitudes deeper than the speckle images. We define a reference set of 88 sources (real stars) in the central $2'' \times 2''$ region with $K < 17.6$ mag (deepest speckle data sets limit) and detected as the same source in at least one-third of 39 AO epochs. The real sources typically have high bootstrap fractions, while the remaining detections have quite low bootstrap fractions. The bootstrap fraction of any given object is defined as

Table 5
Comparison between Speckle Holography version 2_1 and version 2_2

Date		K_{lim} (mag)		$N_{\text{Real Stars}}$		N_{pix}^b		Max Frames		N_{ref}^c	
(U.T.)	(Decimal)	Value ^d	Δm^e	Value	Ratio	Value	Ratio	Value	Ratio	Value	Ratio
1995 Jun 9–12	1995.439	17.0	1.15	41	1.21	108042	0.90	5286	1.24	19	0.95
1996 Jun 26–27	1996.485	15.8	0.36	49	1.40	82505	0.79	2336	0.52	22	1.10
1997 May 14	1997.367	16.8	0.48	51	1.21	92467	0.74	3486	2.99	25	0.83
1998 Apr 2–3	1998.251	15.8	0.25	39	1.00	95816	0.78	1730	0.83	24	0.81
1998 May 14–15	1998.366	16.8	−0.02	45	0.92	102328	0.82	7685	0.77	24	0.89
1998 Jul 3–5	1998.505	16.4	0.57	43	1.08	116557	0.83	2053	0.81	24	0.83
1998 Aug 4–6	1998.590	17.1	0.16	47	0.94	109269	N/A ^f	11047	0.46	23	0.77
1998 Oct 9, 11	1998.771	16.6	0.41	45	1.22	97215	0.81	2015	0.87	24	0.80
1999 May 2–4	1999.333	17.2	0.10	52	0.96	107882	0.77	9427	0.96	22	0.81
1999 Jul 24–25	1999.559	17.4	0.73	54	1.02	100567	0.76	5776	0.99	23	0.79
2000 Apr 21	2000.305	15.7	0.13	56	1.81	96248	0.78	662	0.21	21	0.84
2000 May 19–20	2000.381	17.5	0.39	55	0.89	96853	0.80	15591	0.98	23	0.79
2000 Jul 19–20	2000.584	17.0	0.32	63	1.29	86452	0.78	10678	0.98	23	0.82
2000 Oct 18	2000.797	16.2	0.51	52	1.73	82315	0.84	2247	0.88	17	0.74
2001 May 7–9	2001.351	17.2	0.53	64	1.28	85028	0.91	6678	0.85	21	0.84
2001 Jul 28–29	2001.572	17.4	0.22	74	1.21	96872	0.78	6654	0.99	23	0.85
2002 Apr 23–24	2002.309	17.5	0.65	74	1.30	96953	0.79	13469	0.98	23	0.82
2002 May 23–24	2002.391	17.6	0.51	72	1.22	98552	0.83	11860	0.99	21	0.78
2002 Jul 19–20	2002.547	16.8	0.59	69	1.73	99994	0.79	4192	0.72	22	0.81
2003 Apr 21–22	2003.303	16.4	0.32	58	1.49	90963	0.93	3715	0.89	23	0.96
2003 Jul 22–23	2003.554	16.8	0.25	65	1.41	87265	0.79	2914	0.96	24	0.86
2003 Sep 7–8	2003.682	17.1	0.60	74	1.57	95367	0.79	6324	1.00	20	0.77
2004 Apr 29–30	2004.327	16.8	0.15	58	1.07	125423	0.99	6212	0.51	26	1.00
2004 Jul 25–26	2004.564	17.4	0.48	80	1.45	99819	0.78	13085	0.99	22	0.85
2004 Aug 29	2004.660	16.8	0.60	63	1.54	96172	0.96	2299	0.75	25	0.93
2005 Apr 24–25	2005.312	17.1	0.24	70	1.46	105715	0.81	9644	0.88	24	0.89
2005 Jul 26–27	2005.566	16.8	0.81	84	2.33	108360	0.79	5642	0.96	23	0.92

Notes.

^a K_{lim} is the magnitude that corresponds to the 95th percentile of all K magnitudes in the sample of real stars in the central $2'' \times 2''$ region (see Appendix B.1).

^b N_{pix} refers to the number of pixels in a given image that meet a .8 of maximum frames used criteria.

^c N_{ref} refers to the number of reference stars used to align the epoch of data.

^d All values given in the table are the results of version 2_2.

^e $\Delta m = K_{\text{lim},2_2} - K_{\text{lim},2_1}$, is the detection limit difference between the version 2_2 and the version 2_1. The average magnitude limit has been increased from $K = 16.5$ (version 2_1) to $K = 16.5$ (version 2_2).

^f The number of pixels in 1998 August is removed due to an artifact in the old holography image.

the portion of bootstrap images (among overall 100 bootstraps) in which the object can be detected (see Step 4 in Section 3.5). We use the remaining sources to estimate the surface density of likely spurious detections in the central $2'' \times 2''$ region at each bootstrap fraction, below which the detection is treated as likely spurious. Assuming a random process we can thus compute the probability of obtaining a false detection within 10 mas search radius around its nominal position, which is a function of the bootstrap fraction threshold that is applied to each epoch (see Figure 19). To avoid false detections, we require that the bootstrap fraction cut of a real source detection in each epoch is obtained and has a probability of a false detection within a 10 mas radius that is always $<1\%$. See Table 2 for the summary of the bootstrap fraction cut.

Then the source detection limit for each epoch is determined to be the 95th percentile of all K magnitudes in the sample, which includes all sources with a bootstrap fraction that is higher than the threshold in the central $2'' \times 2''$ FoV. The median of the detection limit for all epochs is 16.9 mag at K , which corresponds to observed flux of 0.15 mJy and dereddened flux of 1.4 mJy, respectively. See Table 2 for details.

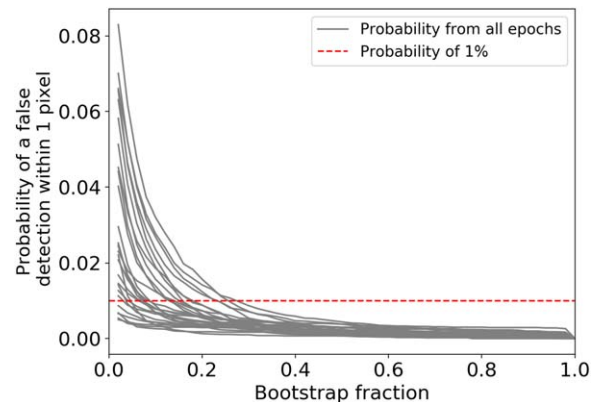


Figure 19. Probability of a false detection within 1 pixel (10 mas square) around its nominal position as a function of bootstrap fraction cut below which the detection is treated as likely spurious. Each gray line presents one epoch's probability function at all possible bootstrap fractions. The bootstrap fraction cut of a real detection in each epoch is set to be the value at which the probability of a false detection within 1 pixel is 1% (red line). This ensures that all detections are real.

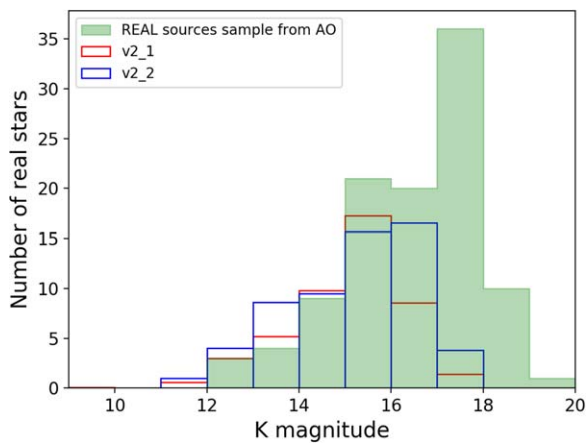


Figure 20. Comparison of the distribution of real detections based on their K -band magnitudes with the original speckle holography (version 2_1, red) and the new implementation presented here (version 2_2, blue). The green histogram shows the distribution of real sources sample defined in Appendix B.1 with their average K' magnitudes from AO observations. The number of real detections for each speckle holography version plotted here is the average from 27 speckle epochs. The new analysis results in deeper detection (~ 0.4 mag deeper), and increases significantly the completeness of detection between $K = 15 \sim 17$ mag, where Sgr A* lies.

B.2. Comparison between Speckle Holography version 2_1 and version 2_2

We performed the real source analysis (see Appendix B.1) for both speckle holography version 2_1 and version 2_2, and then obtained the real source lists for two data sets, respectively. Here we compare speckle holography analysis version 2_1 and version 2_2 based on the real detection list in the central $2'' \times 2''$ region.

1. The speckle holography technique version 2_2 results in deeper detections. The average magnitude limit for speckle data has been increased from $K = 16.5$ (version 2_1) to $K = 16.9$ (version 2_2). See Table 5 for details of each epoch. See Figure 20.
2. In $>80\%$ epochs, the speckle holography technique version 2_2 results in more real detections. The average number of real detected stars in the central $2'' \times 2''$ region has been increased from $N = 46$ (version 2_1) to $N = 59$ (version 2_2). See Table 5 for details of each epoch.
3. The version 2_2 increases the completeness of detection between $K = 15 \sim 17$ mag, where Sgr A* lies (see Figure 20).
4. The halos around sources, especially bright ones, are reduced in the speckle holography version 2_2 data sets (see Section 3.1 and Figure 1).
5. For the speckle holography version 2_1 data sets, we obtain the uncertainties from running StarFinder on three sub-maps (standard deviation divided by square root 3). For the version 2_2 data sets, we calculate the uncertainties from running StarFinder on up to 100 bootstraps. This new bootstrapping technique gives mathematically more accurate uncertainties.

ORCID iDs

Zhuo Chen <https://orcid.org/0000-0002-3038-3896>
 E. Gallego-Cano <https://orcid.org/0000-0002-7452-1496>

T. Do <https://orcid.org/0000-0001-9554-6062>
 G. Witzel <https://orcid.org/0000-0003-2618-797X>
 A. M. Ghez <https://orcid.org/0000-0003-3230-5055>
 J. Lu <https://orcid.org/0000-0001-9611-0009>
 M. R. Morris <https://orcid.org/0000-0002-6753-2066>
 A. Dehghanfar <https://orcid.org/0000-0003-0518-944X>
 A. K. Gautam <https://orcid.org/0000-0002-2836-117X>
 A. Hees <https://orcid.org/0000-0002-2186-644X>
 M. W. Hosek, Jr. <https://orcid.org/0000-0003-2874-1196>
 S. Jia <https://orcid.org/0000-0001-5341-0765>
 A. C. Mangian <https://orcid.org/0000-0003-2385-6904>

References

- Abramowicz, M. A., Chen, X., Kato, S., Lasota, J.-P., & Regev, O. 1995, *ApJL*, 438, L37
- Blum, R. D., Sellgren, K., & Depoy, D. L. 1996, *ApJ*, 470, 864
- Boehle, A., Ghez, A. M., Schödel, R., et al. 2016, *ApJ*, 830, 17
- Diolaiti, E., Bendinelli, O., Bonaccini, D., et al. 2000, *Proc. SPIE*, 4007, 879
- Do, T., Ghez, A. M., Morris, M. R., et al. 2009, *ApJ*, 691, 1021
- Dodds-Eden, K., Gillessen, S., Fritz, T. K., et al. 2011, *ApJ*, 728, 37
- Eckart, A., Baganoff, F. K., Schödel, R., et al. 2006, *A&A*, 450, 535
- Eckart, A., & Genzel, R. 1996, *Natur*, 383, 415
- Eckart, A., Genzel, R., Hofmann, R., et al. 1995, *ApJL*, 445, L23
- Gautam, A. K., Do, T., Ghez, A. M., et al. 2019, *ApJ*, 871, 103
- Genzel, R., Schödel, R., Ott, T., et al. 2003, *Natur*, 425, 934
- Ghez, A. M., Hornstein, S. D., Lu, J. R., et al. 2005a, *ApJ*, 635, 1087
- Ghez, A. M., Klein, B. L., Morris, M., & Becklin, E. E. 1998, *ApJ*, 509, 678
- Ghez, A. M., Morris, M., Becklin, E. E., Tanner, A., & Kremenek, T. 2000, *Natur*, 407, 349
- Ghez, A. M., Salim, S., Hornstein, S. D., et al. 2005b, *ApJ*, 620, 744
- Ghez, A. M., Salim, S., Weinberg, N. N., et al. 2008, *ApJ*, 689, 1044
- Ghez, A. M., Wright, S. A., Matthews, K., et al. 2004, *ApJL*, 601, L159
- Gillessen, S., Eisenhauer, F., Trippe, S., et al. 2009, *ApJ*, 692, 1075
- Gillessen, S., Genzel, R., Fritz, T. K., et al. 2012, *Natur*, 481, 51
- Gillessen, S., Plewa, P. M., Eisenhauer, F., et al. 2017, *ApJ*, 837, 30
- Hora, J. L., Witzel, G., Ashby, M. L. N., et al. 2014, *ApJ*, 793, 120
- Hornstein, S. D., Ghez, A. M., Tanner, A., et al. 2002, *ApJL*, 577, L9
- Hughes, P. A., Aller, H. D., & Aller, M. F. 1992, *ApJ*, 396, 469
- Ichimaru, S. 1977, *ApJ*, 214, 840
- Jia, S., Lu, J. R., Sakai, S., et al. 2019, *ApJ*, 873, 9
- Lu, J. R., Ghez, A. M., Hornstein, S. D., Morris, M., & Becklin, E. E. 2005, *ApJL*, 625, L51
- Markowitz, A., Edelson, R., Vaughan, S., et al. 2003, *ApJ*, 593, 96
- Matthews, K., Ghez, A. M., Weinberger, A. J., & Neugebauer, G. 1996, *PASP*, 108, 615
- Matthews, K., & Soifer, B. T. 1994, *ExA*, 3, 77
- McHardy, I. M., Koeding, E., Knigge, C., Uttley, P., & Fender, R. P. 2006, *Natur*, 444, 730
- Melia, F., & Falcke, H. 2001, *ARA&A*, 39, 309
- Meyer, L., Do, T., Ghez, A., et al. 2008, *ApJL*, 688, L17
- Meyer, L., Do, T., Ghez, A., et al. 2009, *ApJL*, 694, L87
- Meyer, L., Ghez, A. M., Schödel, R., et al. 2012, *Sci*, 338, 84
- Meyer, L., Witzel, G., Longstaff, F. A., & Ghez, A. M. 2014, *ApJ*, 791, 24
- Murray-Clay, R. A., & Loeb, A. 2012, *NatCo*, 3, 1049
- Narayan, R., & Yi, I. 1994, *ApJL*, 428, L13
- Narayan, R., Yi, I., & Mahadevan, R. 1995, *Natur*, 374, 623
- Paltani, S. 1999, in ASP Conf. Ser. 159, BL Lac Phenomenon, ed. L. O. Takalo & A. Sillanpää (San Francisco, CA: ASP), 293
- Pfuhl, O., Gillessen, S., Eisenhauer, F., et al. 2015, *ApJ*, 798, 111
- Phifer, K., Do, T., Meyer, L., et al. 2013, *ApJL*, 773, L13
- Press, W. H. 1978, *ComAp*, 7, 103
- Primot, J., Rousset, G., & Fontanella, J. C. 1990, *JOSAA*, 7, 1598
- Rafelski, M., Ghez, A. M., Hornstein, S. D., Lu, J. R., & Morris, M. 2007, *ApJ*, 659, 1241
- Reid, M. J. 1993, *ARA&A*, 31, 345
- Sakai, S., Lu, J. R., Ghez, A. M., et al. 2019, *ApJ*, 873, 65
- Schartmann, M., Burkert, A., Alig, C., et al. 2012, *ApJ*, 755, 155
- Schödel, R., Morris, M. R., Muzic, K., et al. 2011, *A&A*, 532, A83
- Schödel, R., Najarro, F., Muzic, K., & Eckart, A. 2010, *A&A*, 511, A18
- Schödel, R., Ott, T., Genzel, R., et al. 2002, *Natur*, 419, 694
- Schödel, R., Yelda, S., Ghez, A., et al. 2013, *MNRAS*, 429, 1367
- Simonetti, J. H., Cordes, J. M., & Heeschen, D. S. 1985, *ApJ*, 296, 46

- Sitarski, B., Do, T., Witzel, G., et al. 2014, AAS Meeting, [223](#), [238.05](#)
- Timmer, J., & Koenig, M. 1995, A&A, [300](#), [707](#)
- Tokunaga, A. T. 2000, in Allen's Astrophysical Quantities, ed. A. N. Cox (4th ed.; Melville, NY: AIP), [143](#)
- Uttley, P., & McHardy, I. M. 2005, [MNRAS](#), [363](#), [586](#)
- Uttley, P., McHardy, I. M., & Papadakis, I. E. 2002, [MNRAS](#), [332](#), [231](#)
- Valencia-S, M., Eckart, A., Zajaček, M., et al. 2015, [ApJ](#), [800](#), [125](#)
- Witzel, G., Eckart, A., Bremer, M., et al. 2012, [ApJS](#), [203](#), [18](#)
- Witzel, G., Ghez, A. M., Morris, M. R., et al. 2014, [ApJL](#), [796](#), [L8](#)
- Witzel, G., Martinez, G., Hora, J., et al. 2018, [ApJ](#), [863](#), [15](#)
- Witzel, G., Sitarski, B. N., Ghez, A. M., et al. 2017, [ApJ](#), [847](#), [80](#)
- Yuan, F., Quataert, E., & Narayan, R. 2003, [ApJ](#), [598](#), [301](#)